Grain size dependent martensitic twinning behavior in superelastic Ti-20Zr-12Nb-2Sn alloy: A comparative study

J. J. Gao, P. Castany, T. Gloriant

▶ To cite this version:

J. J. Gao, P. Castany, T. Gloriant. Grain size dependent martensitic twinning behavior in superelastic Ti-20Zr-12Nb-2Sn alloy: A comparative study. Acta Materialia, 2025, 296, pp.121260. ⟨10.1016/j.actamat.2025.121260⟩. ⟨hal-05167550⟩

Acta Materialia 296 (2025) 121260

Contents lists available at ScienceDirect

Acta Materialia

journal homepage: www.elsevier.com/locate/actamat

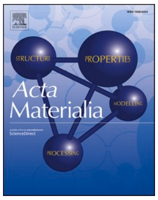

Grain size dependent martensitic twinning behavior in superelastic Ti-20Zr-12Nb-2Sn alloy: A comparative study

J.J. Gao [a,b,*], P. Castany [b,*], T. Gloriant [b]

[a] *School of Materials Science and Engineering, Tianjin University of Technology, Tianjin, 300384, China*
[b] *University Rennes, INSA Rennes, CNRS, ISCR UMR 6226, 35000 Rennes, France*

ARTICLE INFO

Keywords:
Ti-Zr-Nb-Sn
Superelastic Ti alloy
Deformation twinning
Stress-induced martensitic transformation

ABSTRACT

The superelastic Ti-20Zr-12Nb-2Sn (at. %) alloy is investigated before and after deformation by cyclic/conventional tensile tests, optical microscopy, *in situ* synchrotron X-ray diffraction (SXRD), electron back-scattered diffraction (EBSD) and transmission electron microscopy (TEM) after 700 °C and 900 °C solution treatments for 30 min. Both of the specimens show the same $\{111\}\langle 101\rangle_{\beta}$ recrystallization texture, but a different average grain size of respectively 8 µm and 105 µm. Occurrence of the reversible stress-induced martensitic (SIM) α'' transformation is validated through *in situ* SXRD. After plastic deformation, this alloy displays a grain size dependent martensitic twinning behavior. In the fine grain material, only residual SIM α'' phase is observed with no twinning up to rupture, which was never reported in plastically deformed Ti-based superelastic alloys. In the coarse grain material, twins are observed in residual SIM α'' phase. For the 5 % strained specimen, primary/secondary martensitic α'' band undergoes a novel three-step twinning process (primary $\{130\}\langle 310\rangle_{\alpha''}$ twinning + $\langle 211\rangle_{\alpha''}$ type II twinning + secondary $\{130\}\langle 310\rangle_{\alpha''}$ twinning). We also showed that the final product of this three-step process can be misinterpreted as $\{021\}\langle 512\rangle_{\alpha''}$ type II twinning. This primary/secondary α'' twin band is then further partially twinned again by a third $\{130\}\langle 310\rangle_{\alpha''}$ twinning or $\{110\}\langle 110\rangle_{\alpha''}$ twinning at 8 % of strain, highlighting an unprecedented fourth step twinning process. $\{130\}\langle 310\rangle_{\alpha''}$ twins are systematically reorientated by $\langle 211\rangle_{\alpha''}$ type II twinning in order to maximize the transformation strain value with respect to their β phase counterpart. This work comprehensively sheds light on the mechanism of superelasticity optimization via grain size refinement strategy.

1. Introduction

The superelastic NiTi alloys are widely employed for biomedical devices due to their functional properties, such as orthodontic arches, guide wires, stents. However, the cytotoxicity and hypersensitivity of Ni is still an issue for the biocompatibility [1]. Hence, the superelastic β Ti-based alloys with non-toxic elements have been designed and investigated in recent years. Among the developed biomedical titanium alloys, the most extensively studied ones are Ti-Nb based alloys, *i.e.*, Ti-Nb-O [2–6], Ti-Nb-N [3,5], Ti-Nb-Zr [7–10], Ti-Nb-Ta [9], Ti-Nb-Zr-Sn [11,12]. Nonetheless, most of them have less than satisfactory superelastic performance, which is attributed to reversible transformation between the body-centered cubic β phase and the C-centered orthorhombic α'' martensitic phase [5,13–14]. More recently, it is reported that improving Zr content would optimize the martensitic transformation strain [15–20]. A large number of novel Ti-Zr based superelastic alloys are then reported, involving Ti-Zr-Mo-Sn [18], Ti-Zr-Nb-Sn [15,16,19–20], Ti-Zr-Hf-Nb-Sn [21], which exhibit large recovery strains.

In order to improve superelasticity of Ti-based alloys, researchers all over the world have been conducting intense investigations. It is already widely known that the formation of $\{hkl\}\langle 101\rangle_{\beta}$ texture, obtained by combination of severe plastic deformation and recrystallization, is favorable for improving superelasticity [15,16,18,22]. For example, it has been evidenced that the transformation strain along $\langle 101\rangle_{\beta}$ crystallographic orientation is the maximum in the Ti-20Zr-3Mo-3Sn alloy by *in situ* synchrotron X-ray diffraction experiment [18]. Meanwhile, grain refinement is also an alternative route to enhance mechanical properties, such as shape memory effect [23,24], transformation-induced plasticity [25], high strength [26–28], work hardening capability [29], and superelasticity [19,30–33]. More recently, it has been found that the superelasticity of the

---

* Corresponding authors.
E-mail addresses: jingjun_gao@email.tjut.edu.cn (J.J. Gao), philippe.castany@insa-rennes.fr (P. Castany).

https://doi.org/10.1016/j.actamat.2025.121260
Received 6 February 2025; Received in revised form 26 May 2025; Accepted 11 June 2025

Ti-20Zr-12Nb-2Sn alloy decreases with raising grain size even with the same {111}<101>$_\beta$ optimal texture [19], but the underlying mechanism has still not been clearly interpreted.

The residual stress-induced martensitic (SIM) α" phase after deformation and/or twinning is at the origin of the compromising recovery strain during plastic deformation. For the conventional Ti-Nb based alloys, most of the reported deformation products are {332}<113>$_\beta$ [3, 34–37] or {112}<111>$_\beta$ [38–42] twinning. In fact, these two β twinning systems are associated with reversible martensitic transformation. It is widely known that the {332}<113>$_\beta$ and the {112}<111>$_\beta$ twinning recover respectively from {130}<310>$_{\alpha''}$ and {110}<110>$_{\alpha''}$ twinning during the reverse stress-induced martensitic transformation on unloading [34,39,43–44]. Specimen thinning process could also promote this transition, and resulting into the detected β twins instead of martensitic α" twins by transmission electron microscope (TEM) [34, 35]. Chen et al. even captured the orientation relationship of $(130)_{\alpha''}||(332)_\beta$ at the atomic-resolution level in the deformed Ti-Nb-Pb alloy [45]. However, the plastic deformation products and mechanisms are rarely reported about the novel superelastic Ti-Zr based alloys, especially for the Ti-Zr-Nb-Sn alloys behaving large superelasticity [15, 19]. It is therefore necessary to improve our knowledge of plastic deformation for superelastic Ti-Zr-Nb-Sn alloys, and then give a guidance for designing and fabricating high performance Ti-based superelastic alloys.

In the present work, two fully recrystallized Ti-20Zr-12Nb-2Sn specimens behaving the same {111}<101>$_\beta$ texture but with different average grain size (AGS) of 8 μm and 105 μm were obtained. Their plastic deformation microstructures are comparatively investigated using cyclic/conventional tensile tests, optical microscopy (OM), *in situ* synchrotron X-ray diffraction (SXRD), electron back-scattered diffraction (EBSD) and transmission electron microscopy (TEM), and a new grain size dependent martensitic twinning behavior will be evidenced.

2. Materials and methods

The Ti-20Zr-12Nb-2Sn (at. %, Ti20122) ingot was obtained by arc melting under high-purity Ar atmosphere using 99.995 % pure Ti, 99.95 % pure Zr, 99.95 % pure Nb and 99.99 % pure Sn. This ingot was firstly homogenized at 950 °C for 24 h in Ar quartz tube, and then quenched in water. Secondly, cold rolling was conducted until 90 % reduction of the initial thickness. Thirdly, the cold-rolled sheet was machined to dog-bone tensile specimens (3 mm width, 0.5 mm thickness and a gauge length of 15 mm) along rolling direction. Fourthly, tensile specimens were separately solution treated at 700 °C and 900 °C for 30 min (short for ST-700–30 and ST-900–30), followed by water quenching. Finally, the oxidation layer was removed with an acid solution made of 50 % HF and 50 % HNO_3 (vol. %).

Cyclic and conventional tensile tests with a strain rate of 2×10^{-4} s^{-1} using extensometer were employed to quantify the mechanical properties. The tensile direction was paralleled to the rolling direction. For the cyclic tests, the increment was 0.5 % during loading and followed by releasing totally the stress, until 5.0 % of strain. After that, the increment was set at 1.0 % or 2.0 %, and then the stress was removed. The interrupted specimens of ST-700–30 (5 % and 7 % of strain) and ST-900–30 (5 % and 8 % of strain) were obtained from conventional tensile tests for the electron back-scattered diffraction (EBSD) analysis.

The microstructure of the specimens before and after deformation were firstly observed with an Olympus optical microscope. The bulk samples were mechanically mirror-polished by decreasing grades of SiC papers from 800# to 4000#, and then polished by a mixture of colloidal silica suspension and H_2O_2 (7:3). Furthermore, EBSD specimens were prepared by electro-polishing method in a solution (10 % perchloric acid and 90 % methanol, vol. %) at −40 °C and 20 V after mechanical polishing. The microstructure and crystallographic orientation relationships in the gauge region were measured via field-emission gun scanning electron microscopy equipped with EBSD detector (Oxford Instruments Aztec HKL) under an acceleration voltage of 20 kV. The AztecCrystal software was operated for post-processing of the EBSD data.

Transmission electron microscopy (TEM) observation was also conducted with a JEM-2100Plus microscope. TEM thin foils were punched as disks (diameter of 3 mm) and mechanically polished to a thickness of ~50 μm. Twin-jet electropolishing method was applied with a mixture of 6 % perchloric acid and 94 % methanol (vol. %) at −20 °C and stopped before perforation. Specimen final thinning was further performed on an ion milling machine (PIPS II 695, Gatan) until perforation under 6 keV Ar ions, and finished under 1 keV.

In order to unveil the real-time phase transition during tensile tests, the ID22 beamline located at the European Synchrotron Radiation Facility (ESRF, Grenoble, France) was employed for *in situ* synchrotron X-ray diffraction (SXRD) characterization with a wavelength of 0.035453630 nm. The cyclic tensile strain rate was 2×10^{-4} s^{-1} and *in situ* SXRD profiles were acquired at each 0.5 % loading/unloading cycle before 5.0 % of strain, and then the increment was set at 1.0 % or 2.0 % until rupture. The transmitted diffracted beams were collected through a nine-channel detector from 2θ=6° to 2θ=20° for each cycle.

3. Results

Fig. 1a shows the cyclic tensile curves during loading/unloading until 7 % of strain, and conventional curve until rupture of the ST-700–30 specimen. The pseudo-elastic hysteresis loops denote reversible SIM α" phase transformation as previously reported [18–19,46]. The measured recovery strain, the elongation at rupture, ultimate tensile strength and incipient Young's modulus are 3.1 %, 7.1 %, 770 MPa and 45 GPa, respectively. Fig. 1b and 1c display partial *in situ* SXRD profiles during loading and unloading from the interrupted tensile tests at 5 % and 7 %, respectively. As previously reported [19], the ST-700–30 is composed of single β phase before deformation. After being strained to 5 % and 7 %, only SIM α" phase is observed on loading, highlighting the complete phase transition from the initial β phase to the α" phase during tension. After unloading, the $(020)_{\alpha''}$, $(002)_{\alpha''}$, and $(110)_\beta$ peaks are detected, indicating reversible transition from SIM α" phase to β phase except for some residual martensitic α" phase. Besides, the lattice parameters of the two phases are determined as a_β=0.3360 nm, $a_{\alpha''}$=0.3187 nm, $b_{\alpha''}$=0.5043 nm, $c_{\alpha''}$=0.4787 nm.

For the ST-900–30 case in Fig. 2a, hysteresis loops are also evidenced during loading and unloading processes from cyclic curves, but with a lower recovery strain (2.5 %). The measured elongation at rupture, ultimate tensile strength and incipient Young's modulus are 9.5 %, 675 MPa and 56 GPa, respectively. For the *in situ* SXRD results, the initial β phase still transforms into full SIM α" phase on loading at strain of 5 % and 8 %, but more intense martensitic α" peaks are observed after unloading. Meanwhile, except for the reversed parent β phase, it is worth noting that the relative intensity of $(110)_{\alpha''}$, $(020)_{\alpha''}$, $(111)_{\alpha''}$, and $(021)_{\alpha''}$ peaks is increased at 8 %, demonstrating more residual martensitic α" phase in the deformed specimen comparing with 5 % strained sample or with the ST-700–30 alloy. In addition, the lattice parameters of the two phases are measured accurately as a_β=0.3358 nm, $a_{\alpha''}$=0.3145 nm, $b_{\alpha''}$=0.5082 nm, $c_{\alpha''}$=0.4772 nm.

Fig. 3 displays typical optical micrographs of the microstructures observed before and after deformation for ST-700–30 and ST-900–30 specimens. For the undeformed ones in Fig. 3a and 3d, both of the alloys present an equiaxed grain microstructure but with distinct grain sizes: several micrometers for ST-700–30, and several tens of micrometers to more than a hundred micrometers for ST-900–30. After deformation, deformation bands with a width of 0.1~0.5 μm are found inside grains. At low strain (5 %) for ST-700–30 (Fig. 3b), only few bands could be observed. With the strain increased to 7 % (Fig. 3c), numerous deformation bands are visible in most of the grains. For the ST-900–30 at 5 % and 8 % (Fig. 3e-3f), the band density increases and many bands obviously intersect in several grains. The detailed orientations of grains and deformation bands are further studied by EBSD and TEM.

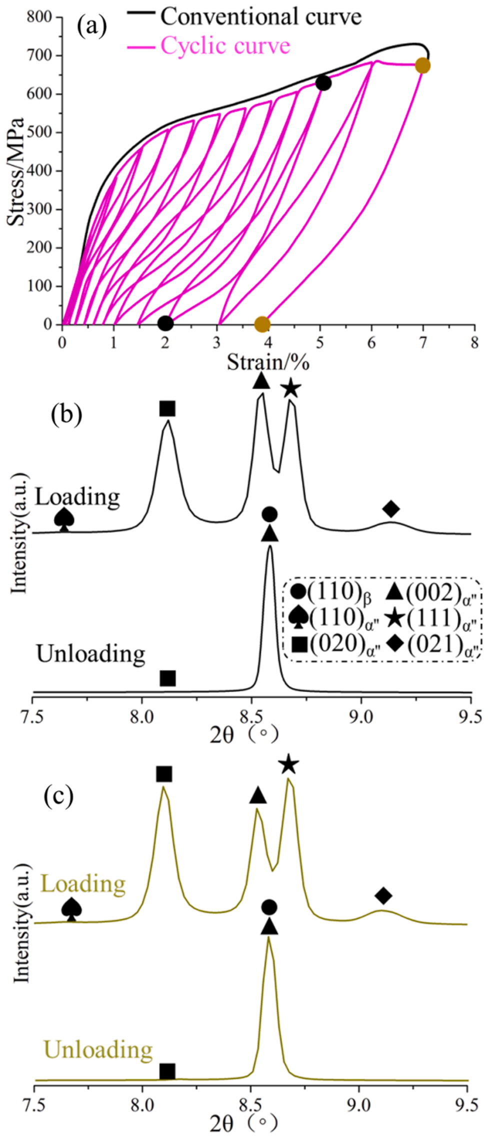

Fig. 1. Cyclic and conventional engineering tensile curves (a) of the ST-700–30 Ti20122 alloy, the corresponding *in situ* SXRD profiles during loading/unloading acquired from the specimens strained to 5 % (b) and 7 % (c).

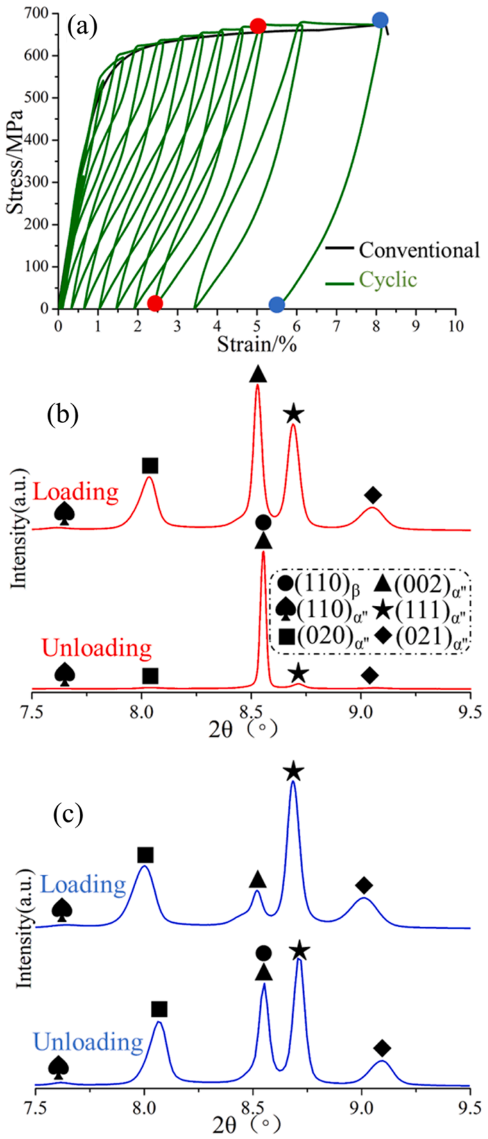

Fig. 2. Cyclic and conventional engineering tensile curves (a) of the ST-900–30 Ti20122 alloy, the corresponding *in situ* SXRD profiles during loading/unloading acquired from the specimens strained to 5 % (b) and 8 % (c).

The recrystallization texture and grain size distribution induced by solution treatments are analyzed by EBSD technique. Fig. 4a and 4c are respectively inverse pole figure (IPF) maps obtained from ST-700–30 and ST-900–30, respectively. Both specimens exhibit the typical equiaxed β-grain microstructure with a predominant green color, indicating {hkl}<101>$_\beta$ preferential orientation. Fig. 4b and 4d are grain size distributions and the averaged grain size is evaluated to be 8 μm and 105 μm, respectively. In order to identify the recrystallization texture precisely, IPFs are given in Fig. 5, where RD is the rolling direction, TD is the transverse direction and ND is the normal direction. Both of the alloys reveal the same {111}<101>$_\beta$ texture, except for a slight {001}<101>$_\beta$ component for the ST-900–30. Therefore, the two solution-treated specimens exhibit a similar grain orientation along the rolling/tensile direction, also shown by a similar density of poles around the <101>$_\beta$ corner of RD IPFs. Meanwhile, phase composition for the undeformed samples is also validated by TEM, as shown in Fig. 6. For the two heat treatments, only the β phase is detected and no nanoscale ω phase formation can be evidenced.

Finally, the major difference that can affect the mechanical properties between the two specimens is grain size. The fine deformation microstructure and the corresponding crystallographic orientation relationships (ORs) are then further investigated comprehensively for the strained specimens by EBSD. A representative grain for each condition is displayed in Fig. 7 for the ST-700–30 specimens strained at 5 % and 7 %. Large scale EBSD maps are available in Sup.1 and Sup.2 of supplementary materials. All of the grains have the same microstructural features than those of grains in Fig. 7. Fig. 7a-c are respectively the typical deformed microstructure shown as band contrast (BC) map, phase map and Euler angle map for ST-700–30 sample after being strained to 5 %. Several needle-like parallel bands are captured, and all of them are indexed as C-centered orthorhombic martensitic α" phase. In order to show a good consistency in this text and improve readability, this SIM α" phase is then named as M1. Fig. 7d-f is the EBSD result of the 7 % strained specimen. It can be noticed that both the number density and width of SIM α" phase are raised due to the increase of deformation compared to 5 %. This SIM α" phase is also labeled as M1 in Fig. 7f. Interestingly, a double orientated SIM α" phase with a misorientation angle of 15° between the two bands' orientations is also captured in the 7 % strained sample, as shown in Fig. 7 g-i. These double orientated plates are respectively labeled as M1A and M1B (Fig. 6i). It should be

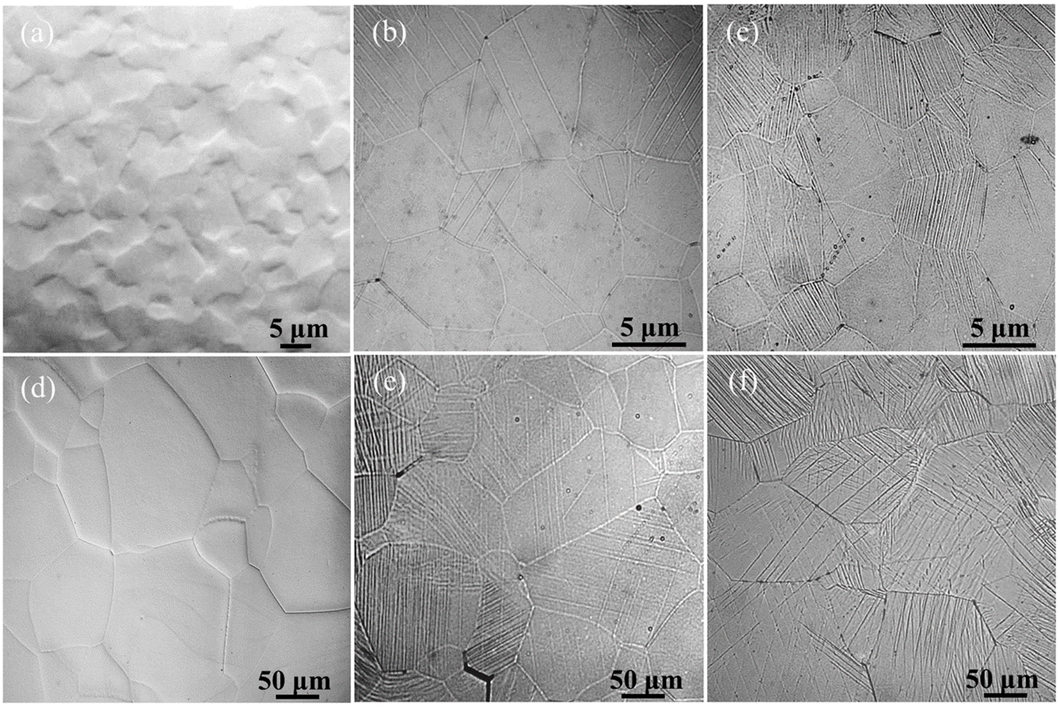

Fig. 3. Optical micrographs of the ST-700–30 (a) and ST-900–30 (d) specimens before deformation, the 5 % (b) and 7 % (c) strained ST-700–30 specimens, and the 5 % (e) and 8 % (f) strained ST-900–30 specimens.

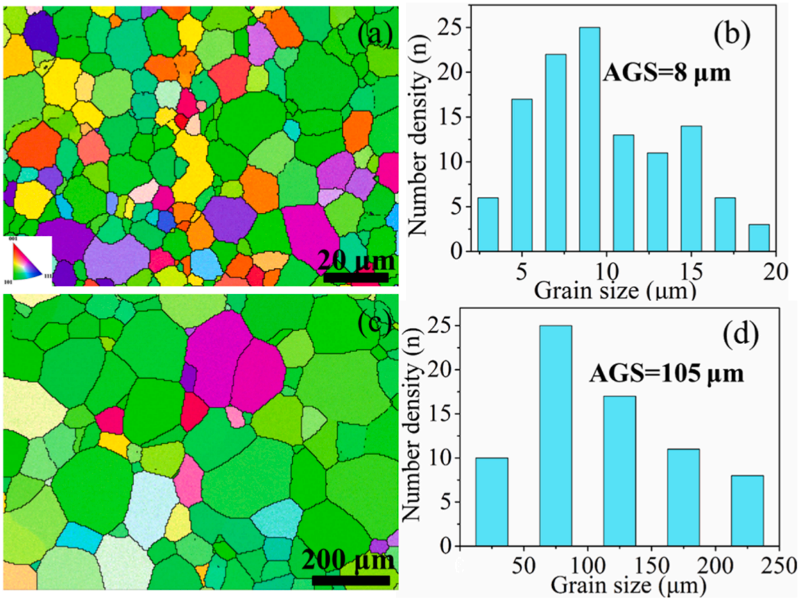

Fig. 4. IPF maps (a,c) along rolling direction and the corresponding grain size distributions (b,d) for ST-700–30 (a-b), ST-900–30 (c-d) specimens.

noted that the frequency of appearance for this double orientated SIM α" phase configuration is quite low (<5 % of grains). The formation mechanism of the aforementioned SIM α" phase both at 5 % and 7 % of strain will be discussed in Section 4.1.

For the ST-900–30 case, a much more complex deformation scenario can be seen. At 5 % of strain, some needle-like α" bands are still visible, but most of them merge to form a large martensitic α" plate, as shown in Fig. 8. Fig. 8d is the enlarged map from Fig. 8c, showing three oriented martensitic plates, namely M1A, M1B and M2. M1A is nearly perpendicular to M1B, which is consistent with OM observation in Fig. 3e, and both have the same crystallographic orientation. Nevertheless, M2 crosses M1A with a misorientation of 23°, and displays a different crystallographic orientation. The detailed ORs will be rationalized in Section 4.2 from stereographic projections. With the strain increasing to 8 % near rupture (Fig. 9), apart from the prevalent needle-like and merged SIM α" phase as reported in Fig. 8, much more deformation bands with a width of ~0.8 µm are triggered (Fig. 9a and 9c). It is interesting to notice some refined microstructures inside the largest deformation bands in Fig. 9d, which is enlarged from Fig. 9c. The distinct crystallographic orientations of SIM α" phase are then respectively labeled as M1A/B, M2 and M3. The deformation mechanisms leading to these different bands will be further clarified in the next

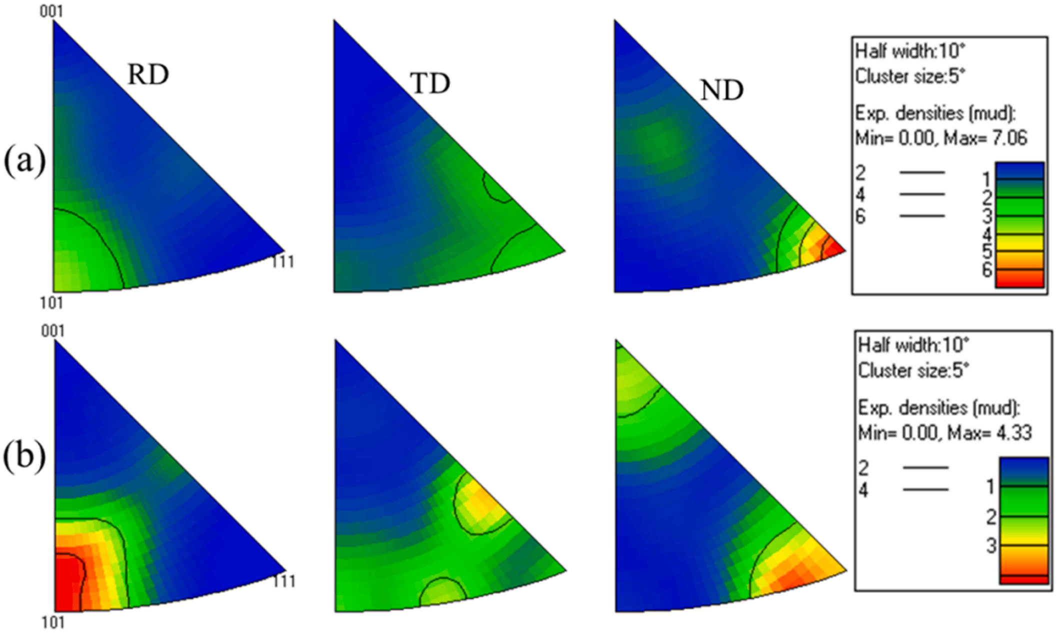

Fig. 5. IPFs of the ST-700–30 (a) and ST-900–30 (b) specimens.

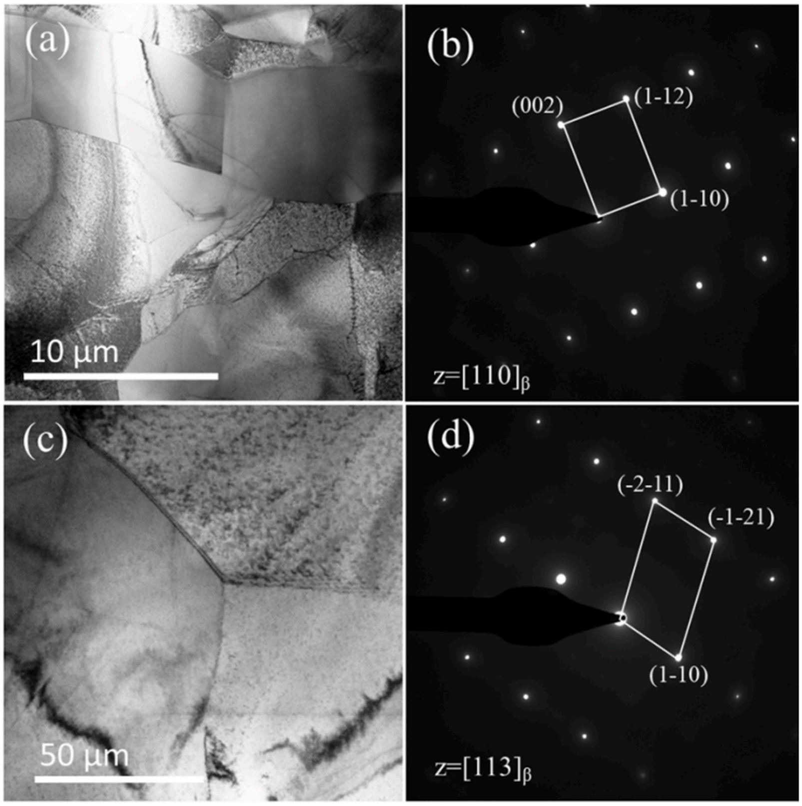

Fig. 6. Bright-field TEM micrographs (a,c), and corresponding electron diffraction patterns (b,d) for the ST-700–30 (a-b) and ST-900–30 (c-d) specimens before deformation.

section. It is noteworthy that M1A/B in Fig. 9d refers to the double orientated SIM α" phase, like M1A and M1B in Fig. 8d at 5 % of strain, but with no significant misorientation between the two types of deformation. This reason will be further explained from stereographic projections in Section 4.2.

4. Analysis and discussion

4.1. Deformation analysis in fine grains (AGS=8 μm)

The Ti20122 alloy displays excellent superelastic behavior attributed to reversible SIM α" transformation. This phase transition process is

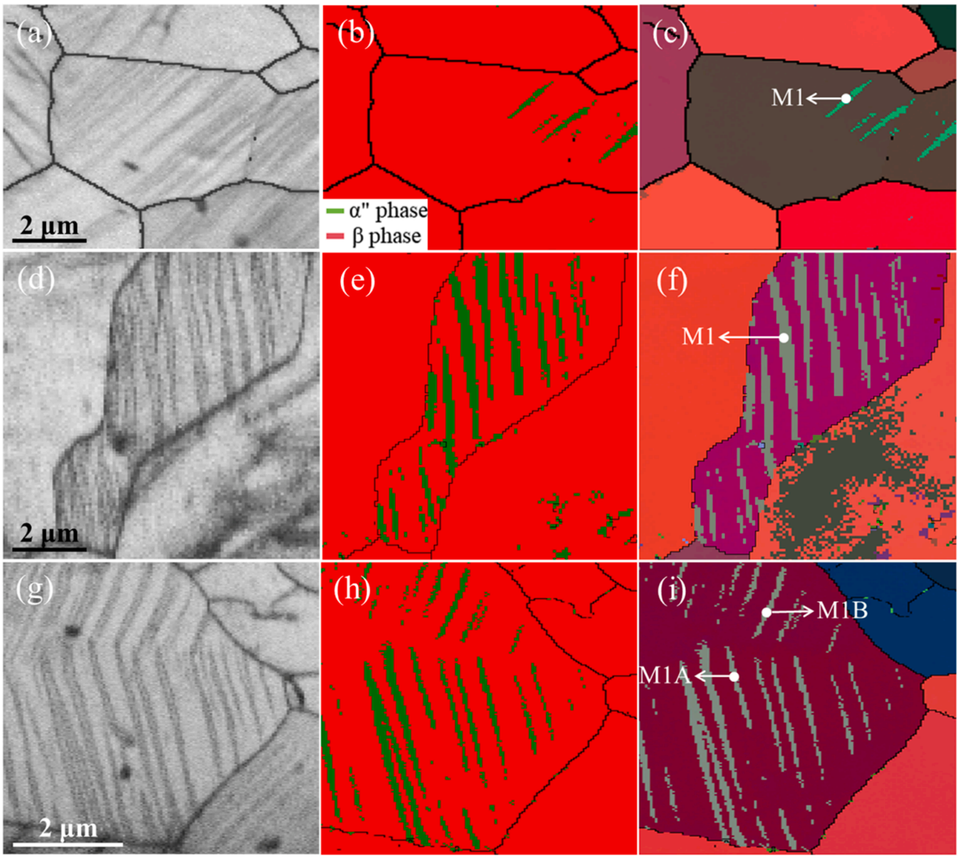

Fig. 7. BCE maps (a,d,g), phase maps (b,e,h), Euler angle maps (c,f,i) of the 5 % (a-c) and 7 % (d-i) strained ST-700–30 specimens.

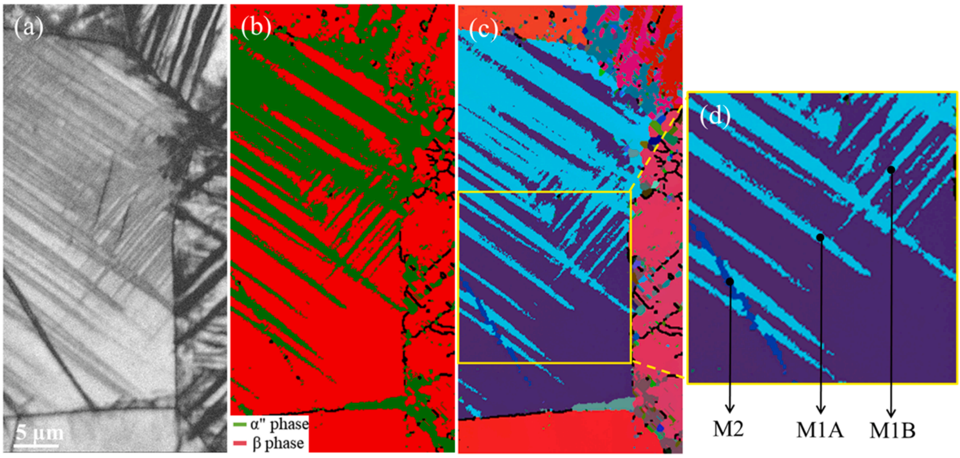

Fig. 8. BCE map (a), phase map (b), Euler angle map (c) of the 5 % strained ST-900–30 specimen, and the zoomed in map (d) from (c) in yellow rectangle.

validated by *in situ* SXRD and residual martensitic α" phase is captured by EBSD during plastic deformation stage (Fig. 7–9). In order to reveal the underlying deformation mechanism, stereographic projections of parent β phase and residual SIM α" phase are thus established in Fig. 10. Solid circles indicate poles of crystallographic planes and open circles represent crystallographic directions. For a better readability, only the three $<100>_{\beta/\alpha"}$ directions and some other related poles and traces of interest are presented. For the 5 % strained specimen of ST-700–30 in Fig. 10a-b, the β matrix and the detected martensitic α" phase exhibit the conventional OR ($[100]_{\alpha"}\|[001]_{\beta}$, $[101]_{\alpha"}\|<111>_{\beta}$), indicating no twinning process occurred during deformation at this stage. This result can also be rationalized by transformation strain calculations in Table 1. The “5 %” column in Table 1 shows the calculated results for each correspondence variant (CV) of martensite. The maximum value is obtained for CV4, which also corresponds to the CV in Fig. 10b For metastable β-Ti alloys, twelve habit plane variants (Table 2) could be formed during martensitic transformation [47–48]. In the present situation, both $(57\text{–}5)_{\beta}$ and $(-575)_{\beta}$ should be equally triggered for CV4. However, the real observed one is only $(-575)_{\beta}$ variant, because its trace is parallel to the interface of the β/α" in Fig. 7a-c. Then, the α" bands observed in Fig. 7a-c are the primary variant of SIM α" phase, which is retained after deformation and without the occurrence of twinning.

At 7 % of strain, the crystallographic orientations of parent β phase and SIM α" phase are respectively displayed by stereographic projections

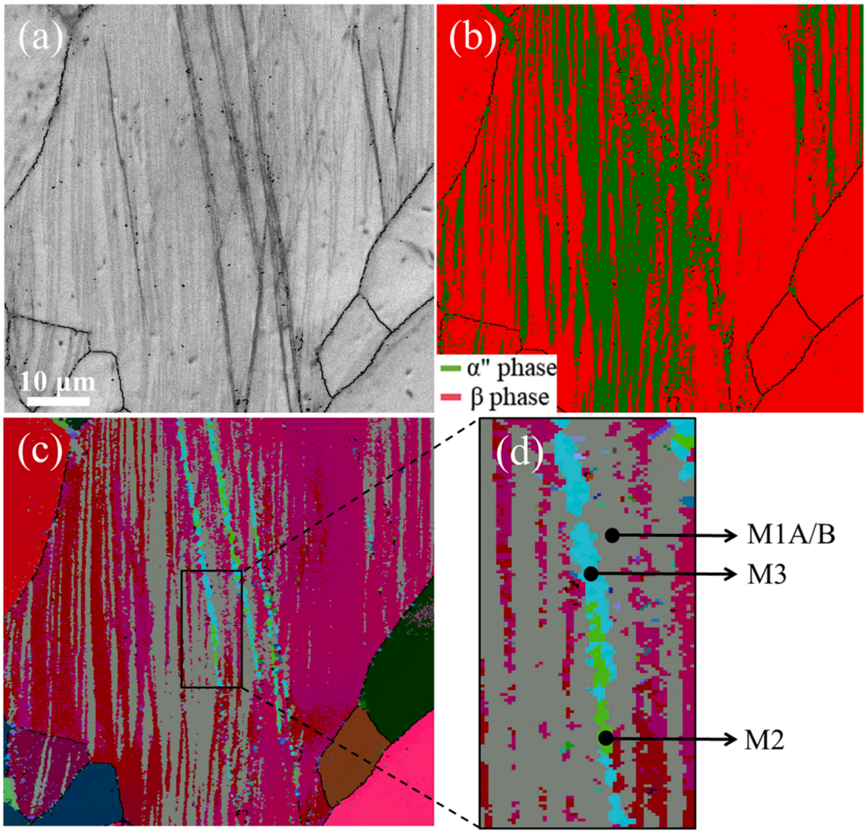

Fig. 9. BCE map (a), phase map (b), Euler angle map (c) of the 8 % strained ST-900–30 specimen, and the zoomed in map (d) from (c) in black rectangle.

in Fig. 10c-e and Fig. 10d-f. The conventional OR between β matrix and SIM α" phase is also detected in both cases. In the first case (Fig. 10c-d), corresponding to the micrograph in Fig. 7d-f, the CV5 is triggered accordingly to the maximum transformation strain of 6.01 % ("7 %−1″ column in Table 1) and the trace of $(557)_\beta$ is parallel to the M1 interface. For the other case, corresponding to the micrograph in Fig. 7 g-i, the orientations of M1A (in black) and M1B (in green) from Fig. 7i are drawn in the Fig. 10f. Besides, it can be seen that the three $<100>_{\alpha''}$ directions almost overlap indicating the same crystallographic orientation, confirming the Euler angle map in Fig. 7i. No twinning relationship is found and only the conventional OR between parent β phase and SIM α" phase is observed. Moreover, the calculated transformation strain values are shown in the "7 %−2" column in Table 1. CV6 reveals the highest value of 6.03 %, which is the actually formed martensitic variant during phase transition. In addition, the traces of both habit plane variants $(-557)_\beta$ and $(5\text{–}57)_\beta$ of CV6 are separately parallel to the interface of M1A and M1B, indicating here the activation of both habit plane variants for CV6.

From the above, the residual SIM α" phase is the main deformation product in the fine grain material. The CV offering the highest transformation strain is only activated with alternatively one or both of the habit plane variant(s). No β/α" twinning systems are detected, *i.e.* there is a twinning-free plastic deformation behavior in these fine grains, which has never been reported in superelastic titanium alloys.

4.2. Deformation analysis in coarse grains (AGS=105 μm)

Fig. 11 exhibits stereographic projections, involving β phase, detected SIM α" phase of M1A/B, M2, and presumed intermediate crystals in ST-900–30 specimen after 5 % of deformation. Fig. 11a and 11c are respectively stereographic projections for the observed β matrix and SIM α" phase of M1A/B, where the black and green color respectively represent M1A and M1B crystals, which have the same crystallographic orientation. The parent β phase (Fig. 11a) keeps conventional OR with SIM α" phase M1A/B (Fig. 11c), and the activated variant is CV4 with the maximum transformation strain value of 5.13 % (Table 1 in the "5 %-M" column). The traces of both potential habit planes, $(-5\text{–}75)_\beta$ and $(-575)_\beta$, for CV4 are nearly perpendicular and are in agreement with the interfaces of M1A and M1B in Fig. 8. For this part of the deformed microstructure, the alloy exhibits the same deformation mechanism as discussed above for the fine grain material.

Fig. 11f is the stereographic projection of the observed M2 band, which obviously has a different crystallographic orientation than M1A/B and does not have the conventional OR with the β matrix. M2 is then not formed directly from β matrix and must be formed via deformation twinning. It is worth noting that such deformation twinning bands are observed in all of the grains of the coarse grain material. According to the trace analysis, the trace of the $(-1\text{–}30)_{\alpha''}$ plane in M1A/B shows a good agreement with the M2 band interface in Fig. 8d, the classical $\{130\}<310>_{\alpha''}$ twinning system thus could be the potential activated one during deformation. The corresponding $(-1\text{–}30)[-310]_{\alpha''}$ twin is then shown in Fig. 11d, as well as the equivalent $(-3\text{–}23)[1\text{–}3\text{–}1]_\beta$ twin in the β phase in Fig. 11b In addition, the real activated twinning variant can be efficiently confirmed by Schmid factor (SF) analysis [35,43,46,49]. The SF values are determined by the following equation: SF=cosλ·cosφ, where λ is the angle between the tensile direction and the normal direction of the twinning plane K_1, and φ is the angle between the tensile direction and the twinning direction η_1. The activated twinning systems of $(-3\text{–}23)[-131]_\beta$ and $(-1\text{–}30)[3\text{–}10]_{\alpha''}$ are therefore approved by the Schmid law because of their maximum value of 0.37 among all variants, as shown in the "SF-5 %" column of Table 3 and in the "SF-1″ column of Table 4. However, the obtained crystallographic orientation of the $(-1\text{–}30)[-310]_{\alpha''}$ twin is not the observed M2 crystal in Fig. 11f. As the M2 orientation does not correspond to any known twinning relationship with M1A/B, the previous $(-1\text{–}30)[3\text{–}10]_{\alpha''}$ twin is probably twinned again. From our previous work [46], such secondary $\{130\}<310>_{\alpha''}$ twinning has been observed after the primary

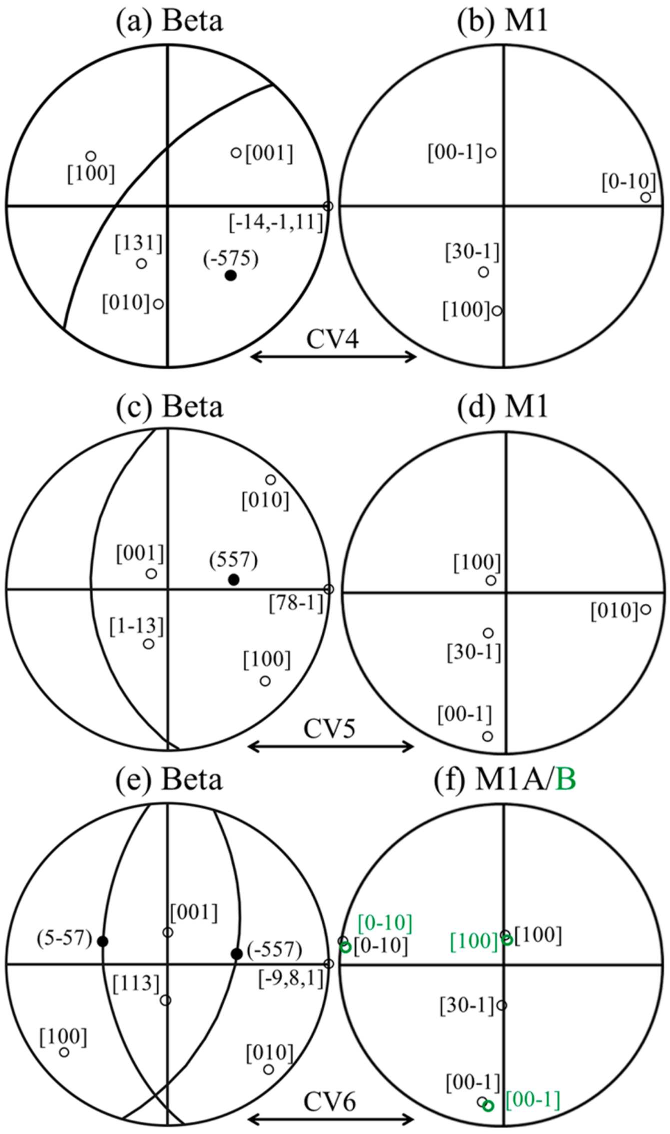

Fig. 10. Stereographic projections of the detected β phase (a,c,e) and SIM α" phase (b,d,f) for the strained 5 % (a-b) and 7 % (c-f) ST-700–30 specimens from Fig. 7c, 7f, and 7i, respectively.

Table 1
The calculated transformation strains for each α" martensitic correspondence variant (the real activated CV in blue).

CV	AGS=8 μm			AGS=105 μm				
	5%	7%-1	7%-2	5%-M	5%-T	8%-M	8%-T	8%-R
CV1	-2.04%	-0.63%	-1.03%	-4.84%	0.52%	-2.54%	**4.99%**	**4.15%**
CV2	-1.67%	0.12%	-1.62%	-5.53%	**6.98%**	-1.56%	0.05%	-0.68%
CV3	0.80%	-1.71%	-0.66%	1.66%	-2.07%	-0.98%	3.42%	-0.91%
CV4	**6.02%**	-1.05%	0.00%	**5.13%**	-2.07%	0.17%	0.28%	3.43%
CV5	0.41%	**6.01%**	0.72%	1.79%	-0.52%	**6.79%**	-1.87%	-.329%
CV6	-0.07%	0.71%	**6.03%**	4.10%	-0.52%	0.44%	-3.99%	-0.40%

$\{130\}<310>_{\alpha''}$ twin has been reorientated by a self-accommodation $\{111\}_{\alpha''}$ type I twinning system. As the $<211>_{\alpha''}$ type II self-accommodation twinning system has also been reported [43,47], the 180° rotation is then applied along $\{111\}_{\alpha''}$ poles, as well as along $<211>_{\alpha''}$ directions in order to find a crystallographic orientation with a $\{130\}_{\alpha''}$ pole in the same position as in the M2 crystal. This process results in the crystal shown in Fig. 11e after a rotation of 180° along the $[2\text{–}11]_{\alpha''}$ direction. However, the crystallographic orientation of this $[2\text{–}11]_{\alpha''}$ twin is still not the observed M2 crystal, but both are sharing a common $\{130\}_{\alpha''}$ pole and a common $<310>_{\alpha''}$ direction. Finally, a rotation of 180° along the $(130)_{\alpha''}$ pole or the $[3\text{–}10]_{\alpha''}$ direction in Fig. 11e leads to the observed M2 crystal (Fig. 11f). In order to validate and rationalize this multiple twinning process, the related transformation strain and SF values are then calculated. After the primary $\{130\}<310>_{\alpha''}$ twinning process, the tensile direction shifts to $[0\ -7\ 6]_{\beta}$ in the β phase (Fig. 11b), which is now the parent β phase. The maximum transformation strain is then computed as 6.98 % for CV2 in the “5 %-T” column of Table 1. However, the $(-1\text{–}30)[-310]_{\alpha''}$ twin in Fig. 11d corresponds to CV4 and leads to a compression (−2.07 %) of the crystal along the tensile direction with respect to its β phase counterpart. Then, $a < 211>_{\alpha''}$ type II reorientation twinning is likely to occur to accommodate this detrimental transformation strain into the most favorable one (6.98 %). Indeed, the $[2\text{–}11]_{\alpha''}$ twin (Fig. 11e) corresponds actually to the CV2 with the maximum value of 6.98 % in $(-3\text{–}23)_{\beta}$ twin (Fig. 11b). Besides, the activated secondary $\{130\}<310>_{\alpha''}$ twinning system between $[2\text{–}11]_{\alpha''}$ twin and M2 crystal is confirmed by SF calculations. In this case, the activated variant is the $(-1\text{–}30)[3\text{–}10]_{\alpha''}$ twin with the maximum SF value of 0.45, as shown in the “SF-2” column of Table 4. Therefore, all of the previously analyzed deformation twinning processes are consistent with a variant selection that obeys both transformation strain values and Schmid law.

It can also be noticed that an alternative OR between M1A/B and M2 can be observed in Fig. 11c and Fig. 11f from the presence of other common poles (in red). Indeed, a common $\{021\}_{\alpha''}$ pole and a common $<512>_{\alpha''}$ direction can be observed and only a rotation of 180° around the common $[-51\text{–}2]_{\alpha''}$ direction allow to find the M2 orientation from M1A/B, showing a type II twinning relationship. However, there are several features that tend to exclude this possibility. Firstly, the trace of the $(0\text{–}2\text{–}1)_{\alpha''}$ twinning plane in Fig. 11c does not match the twin interface observed in the EBSD map (Fig. 8), which is a mandatory condition for a twin. Secondly, this twinning system was predicted by Tobe et al. [50] and, compared to the more classical $\{130\}<310>_{\alpha''}$ twinning, it has a higher shear (0.4678 for $\{021\}<512>_{\alpha''}$ twinning and 0.3536 for $\{130\}<310>_{\alpha''}$ twinning) and requires more atoms to shuffle ($q = 4$ for $\{021\}<512>_{\alpha''}$ twinning and $q = 2$ for $\{130\}<310>_{\alpha''}$ twinning). It appears then less energetically favorable to occur. Similarly, the $<211>_{\alpha''}$ type II self-accommodation twinning is very easy to occur as it is responsible for the reorientation of shape memory alloys. For these reasons, the three-step twinning process is the only reasonable solution to explain the observed M2 twin instead of a direct $\{021\}<512>_{\alpha''}$ type II twinning.

For the 8 % strained specimen after ST-900–30 thermal treatment, the same method is then conducted in order to reveal the twinning processes that lead to the much more complex hierarchical α"

Table 2
The predicted twelve habit plane variants for martensitic α" phase [47].

Variants	Habit Plane	
	(+)	(-)
CV1	$(755)_{\beta}$	$(7\text{–}5\text{–}5)_{\beta}$
CV2	$(7\text{–}55)_{\beta}$	$(75\text{–}5)_{\beta}$
CV3	$(575)_{\beta}$	$(-57\text{–}5)_{\beta}$
CV4	$(57\text{–}5)_{\beta}$	$(-575)_{\beta}$
CV5	$(557)_{\beta}$	$(-5\text{–}57)_{\beta}$
CV6	$(-557)_{\beta}$	$(5\text{–}57)_{\beta}$

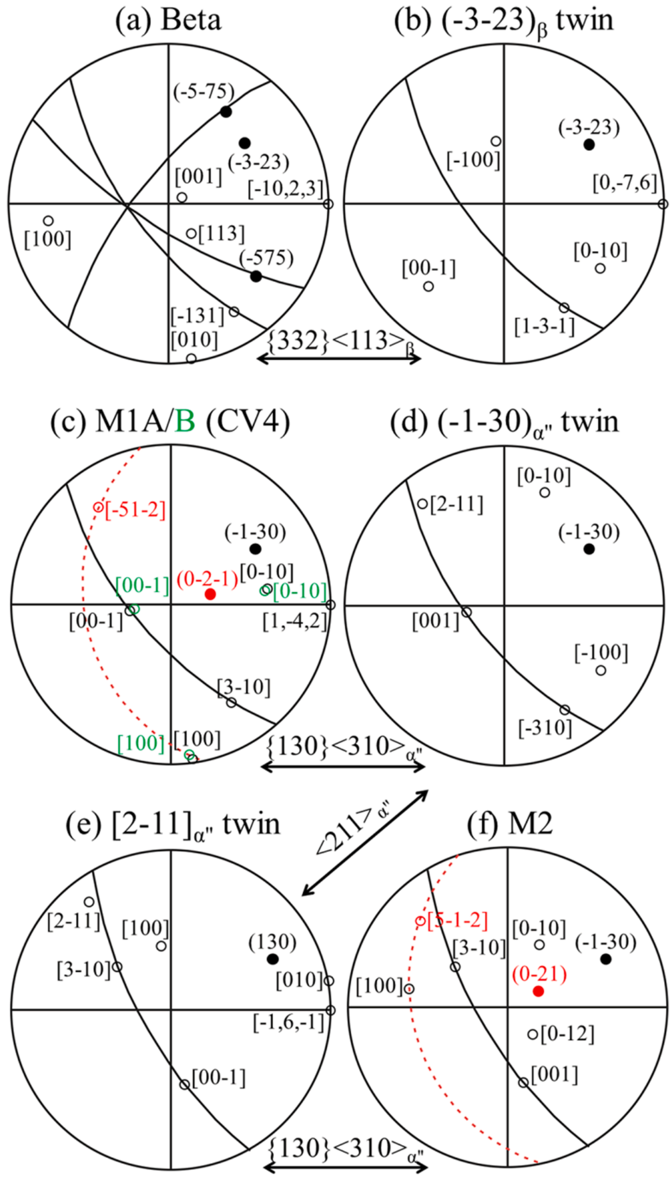

Fig. 11. Stereographic projections of the detected β phase (a), deduced $(-3\text{–}23)[-131]_\beta$ twin (b), the observed SIM α" phase for M1A/B (c), deduced $(-1\text{–}30)[3\text{–}10]_{\alpha''}$ twin (d), deduced $[2\text{–}11]_{\alpha''}$ twin (e), and the observed SIM α" primary band M2 (f) from Fig. 8d.

microstructure of Fig. 9. The Fig. 12a, 12c, 12f are respectively the stereographic projections of the detected parent β phase, SIM α" phase M1A/B and M2. The M1A/B crystal has a conventional OR with β matrix and corresponds to the CV5, which has the highest transformation strain value of 6.79 % (column "8 %-M" in Table 1). Despite the difficulty in distinguishing the two habit plane variants from the EBSD result in Fig. 9c, the two habit plane variants $(557)_\beta$ and $(-5\text{–}57)_\beta$ appear to be observed by stereographic projection. Indeed, their traces, shown in Fig. 12a, are very close, resulting in a small misorientation angle between the two habit plane variants. This is the reason why this crystallographic orientation was labeled "M1A/B" in Fig. 9d and Fig. 12c. This part of the microstructure is then consistent with the deformation mechanism for 5 % of strain in the coarse grain material, as well as 5 % and 7 % in the fine grain material.

Table 3
Twinning elements and calculated Schmid factor values of each variant for the $\{332\}\textless 113\textgreater_\beta$ twinning system at strain of 5 % and 8 % in coarse grains (the real activated variant in blue).

Variants	K_1	η_1	SF-5%	SF-8%	SF-8%-R
V1	$(332)_\beta$	$[11\text{-}3]_\beta$	0.17	**0.45**	-0.23
V2	$(323)_\beta$	$[1\text{-}31]_\beta$	0.12	-0.26	-0.14
V3	$(233)_\beta$	$[\text{-}311]_\beta$	-0.10	-0.34	**0.47**
V4	$(3\text{-}32)_\beta$	$[11\text{-}3]_\beta$	0.35	0.00	0.27
V5	$(3\text{-}23)_\beta$	$[131]_\beta$	0.01	0.11	-0.01
V6	$(2\text{-}33)_\beta$	$[\text{-}3\text{-}11]_\beta$	-0.30	0.14	-0.02
V7	$(\text{-}332)_\beta$	$[\text{-}11\text{-}3]_\beta$	0.07	-0.01	-0.35
V8	$(\text{-}323)_\beta$	$[\text{-}1\text{-}31]_\beta$	0.17	0.24	-0.08
V9	$(\text{-}233)_\beta$	$[311]_\beta$	-0.49	0.01	-0.03
V10	$(33\text{-}2)_\beta$	$[113]_\beta$	-0.02	0.29	-0.19
V11	$(\text{-}3\text{-}23)_\beta$	$[\text{-}131]_\beta$	**0.37**	-0.26	0.44
V12	$(23\text{-}3)_\beta$	$[\text{-}31\text{-}1]_\beta$	-0.37	-0.37	-0.11

Table 4
Twinning elements and calculated Schmid factor values of each variant for the $\{130\}\textless 310\textgreater_{\alpha''}$ twinning system at strain of 5 % and 8 % in coarse grains (the real activated variant in blue).

Variants	K_1	η_1	SF-1	SF-2	SF-3	SF-4	SF-5
V1	$(\text{-}1\text{-}30)_{\alpha''}$	$[3\text{-}10]_{\alpha''}$	**0.37**	**0.45**	**0.45**	**0.05**	0.04
V2	$(1\text{-}30)_{\alpha''}$	$[\text{-}3\text{-}10]_{\alpha''}$	0.24	0.34	0.36	0.44	**0.47**

For the analysis of the stress-induced primary/secondary martensitic α" twin band M2 and the tertiary martensitic α" twin band M3, their stereographic projections are provided in Fig. 12f and Fig. 13d, respectively. On the one hand, the formation of M2 can be explained by the same process than in the 5 % strained specimen. From the crystallographic orientation of M1A/B, a primary $(130)_{\alpha''}$ twin is activated (Fig. 12d), corresponding to the $(332)_\beta$ twin in β phase (Fig. 12b), because the $(130)_{\alpha''}$ trace is parallel to the interface of deformation bands with M1A/B in Fig. 9d This step is supported by the SF values of 0.45 for $(332)[11\text{–}3]_\beta$ and $(130)[-310]_{\alpha''}$ twin variants ("SF-8 %" column of Table 3 and "SF-2″ column of Table 4). However, this $(130)_{\alpha''}$ twin orientation doesn't match either the M2 crystal in Fig. 12f or the M3 crystal in Fig. 13d As for the aforementioned 5 % sample in the coarse grain material, a reorientation of the $(130)_{\alpha''}$ twin by the self-accommodation $[-21\text{–}1]_{\alpha''}$ type II twinning system is proposed (Fig. 12e). As a $\{130\}_{\alpha''}$ pole and a $< 310>_{\alpha''}$ direction are shared between Fig. 12e and Fig. 12f, a rotation of 180° along the $(-1\text{–}30)_{\alpha''}$ pole or the $[-310]_{\alpha''}$ direction is applied on the $[-21\text{–}1]_{\alpha''}$ twin (Fig. 12e), that leads to the M2 orientation (Fig. 12f). These multiple twinning processes can also be explained by transformation strain and SF. The $(130)_{\alpha''}$ twin (Fig. 12d), which is an intermediate state during the whole twinning processes, is activated as CV5 and corresponds to a

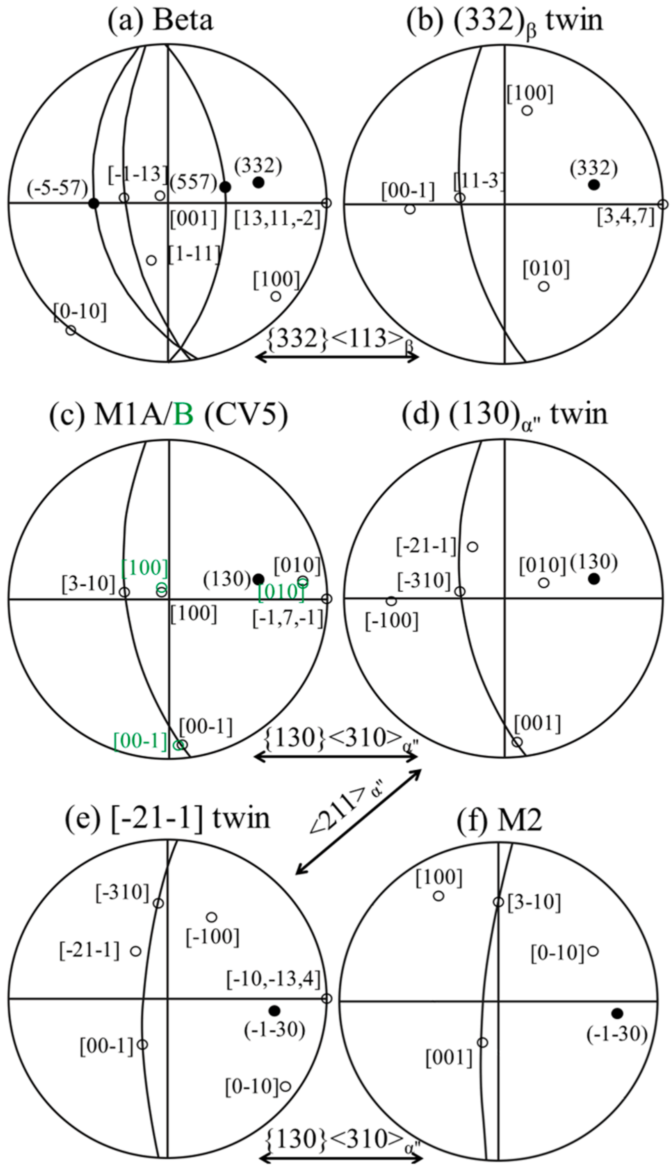

Fig. 12. Stereographic projections of the detected β phase (a), deduced (332)[−1–13]$_{\beta}$ twin (b), the observed SIM α'' phase for M1A/B (c), deduced (130)[3–10]$_{\alpha''}$ twin (d), deduced [−21–1]$_{\alpha''}$ twin (e), the observed SIM α'' primary band M2 (f) from Fig. 9d.

compression of the parent β crystal (Fig. 12b, and −1.87 % transformation strain in “8 %-T” column in Table 1). Reorientation is then favored to produce CV1, which has the maximum transformation strain value of 4.99 % (“8 %-T” column in Table 1). Next, the secondary {130}<310>$_{\alpha''}$ twinning is activated, resulting in the M2 crystal. The difference with the 5 % strained specimen (Fig. 11) is that the secondary {130}<310>$_{\alpha''}$ twinning does not obey the Schmid law: the observed (−1–30)[3–10]$_{\alpha''}$ twin does not have the maximum SF value (0.05 in the “SF-4” column of Table 4). This is probably due to internal stresses caused by the high deformation rate and means that the Schmid law is not sufficient to predict the twin variant activation for this deformation state, whereas maximizing the transformation strain still allows reorientation twinning to be predicted.

On the other hand, the M3 crystallographic orientation corresponds to a new step. Its formation can be explained from the M2 crystal, which is re-presented in Fig. 13c with the observed M3 twin band in Fig. 13d and their β phase counterparts (Fig. 13a-b). It is noticeable that the two crystals share a common {130}$_{\alpha''}$ pole and a common <310>$_{\alpha''}$ direction.

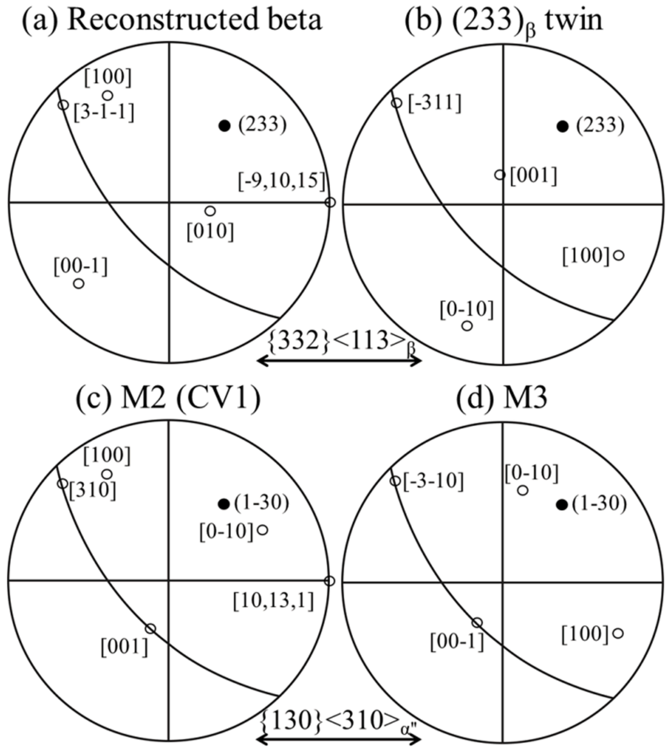

Fig. 13. Stereographic projections of the reconstructed β phase (a) from (c), deduced (233)[3–1–1]$_{\beta}$ twin (b), the observed SIM α'' primary band M2 (f) and secondary band M3 (d) from Fig. 9d.

A 180° rotation around either the (1–30)$_{\alpha''}$ twinning plane or the [310]$_{\alpha''}$ twinning direction leads from Fig. 13c to Fig. 13d, confirming this {130}<310>$_{\alpha''}$ twinning relationship between M2 and M3. In order to validate this twinning process, the β matrix is reconstructed in order to calculate transformation strain values and confirm the correspondence with the (233)[−311]$_{\beta}$ twin (Fig. 13a-b). Based on transformation strain calculation along the [−9 10 15]$_{\beta}$ tensile direction, the CV1 (4.15 % in the “8 %-R” column of Table 1) is the most favorable CV, which is actually the M2 orientation. As M2 is already the best orientated CV, no self-accommodation twinning reorientation process is required as in the previous steps and M2 can directly twin again with the {130}<310>$_{\alpha''}$ twinning system. SF factors are then calculated for M2 and its β phase counterpart, highlighting a maximum value for (223)[−311]$_{\beta}$ (“SF-8 %-R” column in Table 3) and (1–30)[−3–10]$_{\alpha''}$ (“SF-5” column in Table 4) variants, which is the one observed. Twinning for this last step obeys then the Schmid law.

Then, all the observed crystallographic orientations of SIM α'' phase can be explained from the classical {130}<310>$_{\alpha''}$ twinning combined with self-accommodation <211>$_{\alpha''}$ type II reorientation twinning. When {130}<310>$_{\alpha''}$ deformation twins are formed, they always are reorientated before to twin again if their CV is not the one giving the maximum strain. Primary {130}<310>$_{\alpha''}$ twinning formation always obeys the Schmid law, while secondary {130}<310>$_{\alpha''}$ twinning sometimes does not obey Schmid law at high strain levels. Up to four successive twinning steps are recorded to form the M3 crystallographic orientation. Such complex martensitic twinning behavior has never been reported in superelastic Ti-based alloys.

Finally, the deformation products are also verified by TEM (Fig. 14). The Fig. 14(a,c,e) are respectively the bright-field images from 7 % deformed ST-700–30 sample, 5 % and 8 % deformed ST-900–30 samples. Fig. 14(b,d,f) are respectively the corresponding electron diffraction patterns from circled areas in Fig. 14(a,c,e). The associated dark-field images corresponding to circled spots in Fig. 14(b,d,f) are shown in Sup.3–5 of supplementary materials. All the deformation bands are

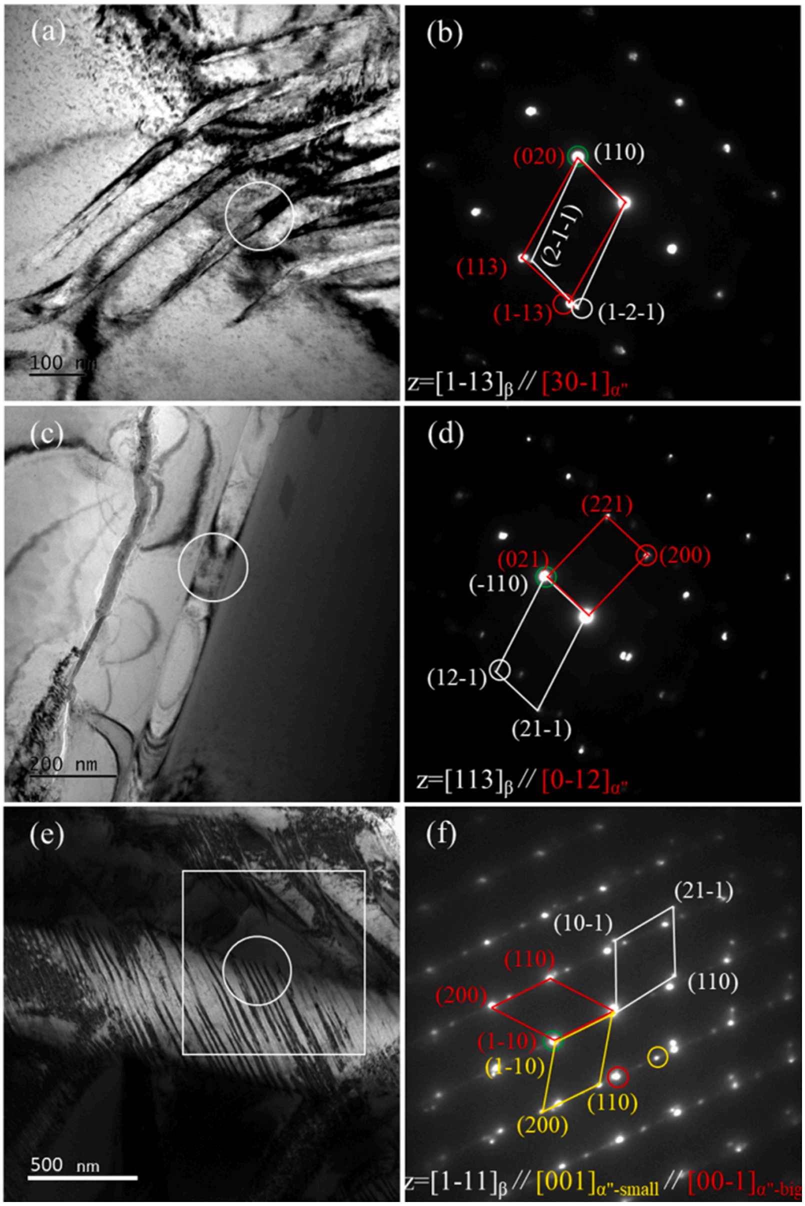

Fig. 14. Bright-field TEM micrographs (a,c,e), and corresponding electron diffraction patterns (b,d,f) for the ST-700–30 specimen deformed at 7 % (a-b), and ST-900–30 (c-f) specimen deformed at 5 % (c-d) and 8 % (e-f).

indexed as the C-centered orthorhombic α" martensitic phase, and no nanoscale ω phase is detected in the deformed samples, as in the initial microstructure. Furthermore, the ORs between the β matrix and SIM α" bands are detailed in Fig. 15. All ORs are the same than those obtained from EBSD (Fig. 10–13). For an easier comparison, all the zone axis directions of TEM observations (Fig. 14b,d,f) are reported in the previous stereographic projections obtained from EBSD analysis (Fig. 10–13). The deformed ST-700–30 specimen only shows stress-induced martensite with the classical OR and two habit plane variants can be also observed by TEM (Fig. 15a,b) as for EBSD results (Fig. 10). In the same way for the ST-900–30 specimens deformed at 5 %, the martensitic band observed by TEM (Fig. 15d) has the same OR with the β matrix (Fig. 15c) than M2 with the matrix in Fig. 11(a,f) obtained from EBSD data. This is particularly evidenced by the correspondence of the $[113]_{\beta}$ direction of the matrix with the $[0–12]_{\alpha''}$ direction of the martensitic twin. This β/M2 OR also leads to the correspondence of the $[1–11]_{\beta}$ direction of the matrix with the $[001]_{\alpha''}$ direction of the martensitic twin shown in the TEM observation of the ST-900–30 specimens deformed at 8 % (Fig. 15e,f for TEM and Fig. 12a,f for EBSD). However, the tertiary twins M3 observed inside the secondary twin M2 differ: While $\{130\}<310>_{\alpha''}$ tertiary twins are observed by EBSD, $\{110\}<110>_{\alpha''}$ tertiary twins are observed by TEM. This twinning OR is obviously evidenced from the common $\{110\}_{\alpha''}$ spots and the common $[001]_{\alpha''}$ zone axis observed in the electron diffraction pattern of Fig. 14f. Although this twinning system is more rarely reported than the $\{130\}<310>_{\alpha''}$, it is an alternative twinning system in β titanium alloys [39,44]. These nanoscale $\{110\}<110>_{\alpha''}$ twins are difficult to be distinguished by EBSD technique due to their very small size, while $\{130\}<310>_{\alpha''}$ are slightly larger to be detectable by EBSD. Therefore, the TEM results confirm the multi-step martensitic twinning process occurring in the coarse grain material and point out the possibility of two potential twinning systems for tertiary twinning for high strain levels: $\{130\}<310>_{\alpha''}$ or $\{110\}<110>_{\alpha''}$.

4.3. *Grain size dominated deformation behavior*

Both of the recrystallized Ti20122 alloys after ST-700–30 and ST-900–30 thermal treatments reveal the same $\{111\}<101>_{\beta}$ texture with

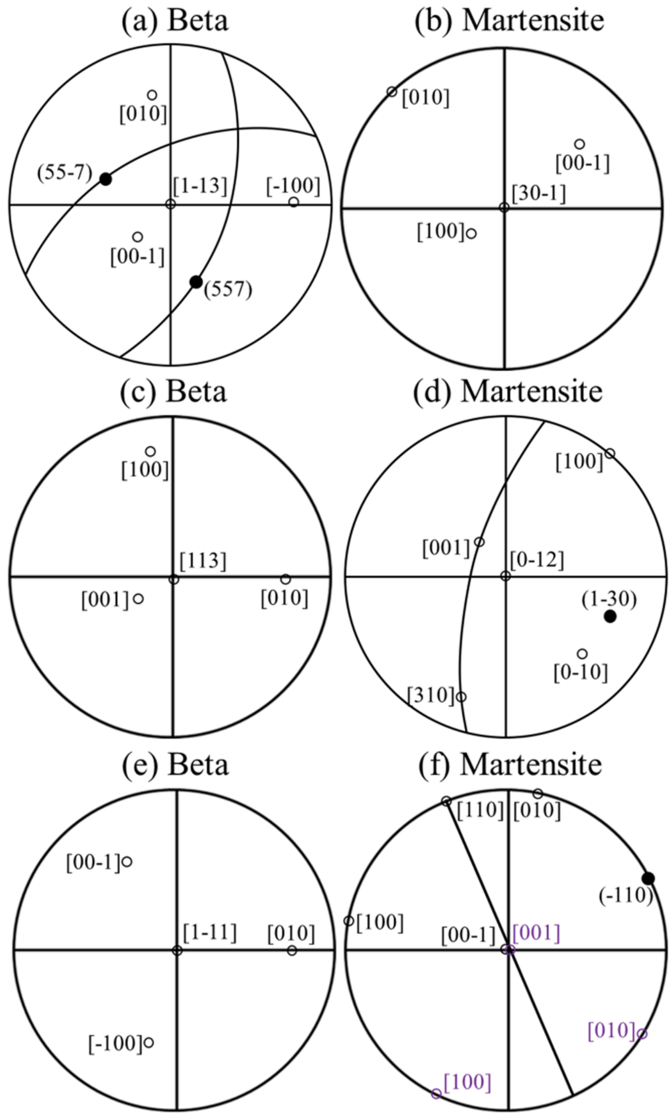

Fig. 15. Stereographic projections of the detected β phase (a,c,e), and martensitic phase (b,d,f) from Fig. 14, where purple circle for small bands.

single β phase, but significant different grain sizes, as shown in Fig. 4 and Fig. 5. After plastic deformation, comparable deformation microstructures and deformation mechanisms are progressively activated in fine (AGS=8 μm) and coarse (AGS=105 μm) grains at the early stages of deformation, whereas complex twinning processes only occur in the coarse grain material, as shown in Fig. 16.

In fine grains (AGS=8 μm), a reversible SIM α" transformation is observed by *in situ* SXRD experiment in Fig. 1, as widely reported in the literature [5,14,18–19,34,35,39]. The SIM α" variant with the maximum transformation strain is activated, and the initial β phase transform into a single CV at the early stage of deformation. When the strain released, the SIM α" phase reverses back to the parent β phase and results in a total recovery of strain. Throughout the entire deformation process until rupture, one or the two possible potential habit plane variant(s) is/are triggered (Fig. 16a,c). Once unloaded, the SIM α" phase transforms back to the parent β phase, and some residual martensite parts remain, highlighting the habit planes as the interfaces with the β phase (Fig. 16b, d). With the strain of 7 % (near rupture), more residual SIM α" phase is visible (Fig. 16d). It can be noticed that grains with a double oriented SIM α" phase have a low observation frequency compared to grains with a single habit plane variant (Fig. 7 g-i). In fact, the formation energy is equal for the activation of one or two habit plane variant(s) [47], and the reason of activation of the two habit plane variants remains unclear. It is worth to note that deformation twinning is not detected whatever the applied strain (5 % and 7 %). Plastic deformation would then only be accommodated by dislocations, resulting in residual SIM α" phase after deformation. The fine grain material then exhibits a twinning-free plastic deformation behavior.

In coarse grains (AGS=105 μm), the same reversible SIM α" transformation occurs (Fig. 2b-c) and the most favorable CV is also formed in the bulk before the plastic deformation stage, as in the small grain material. The two habit plane variants are also sometimes observed. However, a remarkable difference is the observation of deformation twins accompanied with residual SIM α" phase for the plastically deformed specimens. Deformation twins can be detected from the abnormal OR with β matrix and undergo a complex process of multiple twinning. At 5 % of strain, the observed α" twins are not formed by a direct one step $\{130\}<310>_{\alpha''}$ or $\{110\}<110>_{\alpha''}$ twinning, like reported in our previous work [34,39]. Instead, a complex three-step twinning process occurs: (i) the SIM α" phase is twinned by a primary conventional $\{130\}<310>_{\alpha''}$ twinning system; (ii) this $\{130\}<310>_{\alpha''}$ primary twin is then fully reorientated by $a<211>_{\alpha''}$ type II self-accommodation twinning system; (iii) this reorientated primary twin is immediately and completely deformed by a secondary $\{130\}<310>_{\alpha''}$ twinning system (Fig. 16e). When stress released, the parent α" phase reverses back to the β matrix, but the residual SIM α" phase and these three-step twinned bands are thus observed (Fig. 16f). Meanwhile, this reorientated $\{130\}<310>_{\alpha''}$ twin via $<211>_{\alpha''}$ self-accommodation twinning system has also been reported in a fully martensitic α" shape memory alloy [43], but never in superelastic Ti-based alloys.

With the strain increased to 8 % (near rupture), a tertiary $\{130\}<310>_{\alpha''}$ or $\{110\}<110>_{\alpha''}$ twinning system partially occurs inside the previous primary/secondary twins (Fig. 16 g-h), leading to the coexistence of primary/secondary α" twins and tertiary α" twins linked by a $\{130\}<310>_{\alpha''}$ or $\{110\}<110>_{\alpha''}$ twinning relationship. Then, a four-step twinning process is activated at this deformation stage, *i.e.* primary $\{130\}<310>_{\alpha''}$ twinning, $<211>_{\alpha''}$ type II twinning, secondary $\{130\}<310>_{\alpha''}$ twinning, and the third $\{130\}<310>_{\alpha''}$ or $\{110\}<110>_{\alpha''}$ twinning. It should be noted that in all the cases reported, $\{130\}<310>_{\alpha''}$ primary twins are always reorientated because they do not correspond to the CV with the highest transformation strain, but secondary twins do not require reorientation because they directly behave the CV with the highest transformation strain. However, the activation of $\{130\}<310>_{\alpha''}$ twinning obeys the Schmid law in most cases but some deviations can be detected. Then, the maximization of the transformation strain appears as a stronger condition than the SF to predict each twinning step of the process. This complex four-step twinning process is reported here for the first time in superelastic titanium alloys.

Grain size plays a crucial role on activation of deformation twins and it is widely accepted that the critical stress to initiate twinning depends on grain size, as described by the Hall-Petch equation [51–54]. Consequently, twinning has been shown to be suppressed when grain size is reduced in several alloys, such as Mg alloys [51,55], austenitic steels [56,57] and high-entropy alloys [58,59]. The same effect has been observed in metastable β Ti alloys [53,54,60,61] with a decrease of twinning activity in small grain materials compared to coarse grain materials. However, a total suppression of twinning, as reported in the present work, was never reported before. The most accepted reason to explain such dependence of twinning activation on grain size is the accumulation of geometrically necessary dislocations (GND) along grain boundaries, which increases the critical shear stress for twinning due to the subsequent internal stress [59,62]. Kernel Average Misorientation (KAM) is a common way to estimate the density of GND from EBSD data [63]. Such KAM maps are then available in Sup.6 of supplementary materials, for both fine grain and coarse grain Ti-20Zr-12Nb-2Sn alloy, showing a higher density of GND for the small grain condition. Suppression of twinning in the Ti-20Zr-12Nb-2Sn alloy is then most likely due to the higher density of GND in the small grain material compared to

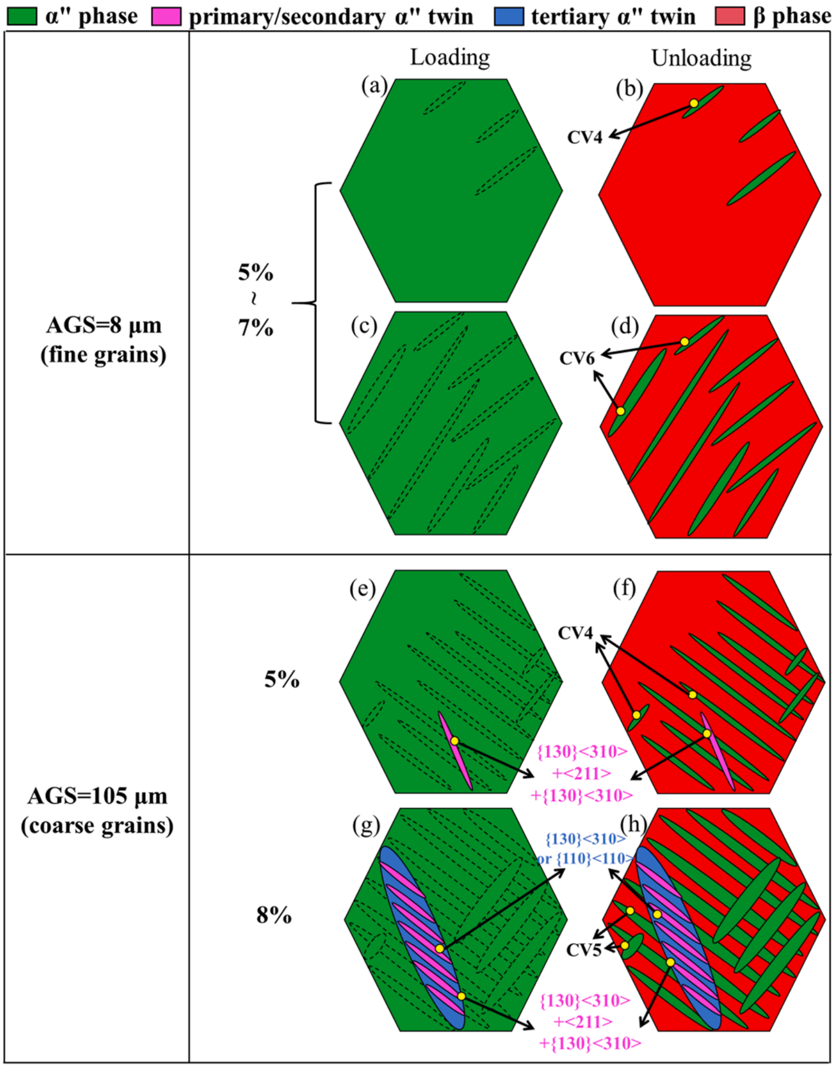

Fig. 16. Schematic illustration of microstructure evolution during plastic deformation for the 5 % (a-b) and 7 % (c-d) strained ST-700–30 specimens, the 5 % (e-f) and 8 % (g-h) strained ST-900–30 specimens during loading (a,c,e,g) and unloading (b,d,f,h).

the coarse grain material, as commonly admitted for other alloys [59,62,63].

It is now clear that the deformation bands observed by OM in fine grains (Fig. 3c-3d) are from residual SIM α" phase and not twins. This twinning-free deformation behavior can explain the improved superelastic performance and strength with grain size refinement (Fig. 1a), compared to the coarse grain material (Fig. 2a). Indeed, plastic deformation and thus residual strain after deformation could be reduced by suppressing twinning in the fine grain material. This grain size dependent martensitic twinning behavior has never been reported up to date.

4.4. *Specific features of twinning*

The deformation behavior of the investigated Ti20122 alloy shows several unprecedented deformation features compared to the previously reported superelastic Ti-based alloys. Firstly, deformation twinning systems, including $\{332\}\langle 113\rangle_{\beta}$, $\{112\}\langle 111\rangle_{\beta}$, $\{130\}\langle 310\rangle_{\alpha''}$ and $\{110\}\langle 110\rangle_{\alpha''}$, are commonly observed in the plastically deformed alloys [34,37–39,41,43,45], whereas no twinning is found in the Ti20122 fine grain alloy. Secondly, the reported β/α" twins are usually only direct primary twins [34,36–41,45,49,54,60], with few reports of secondary twins within primary twins [35,43,46]. Nevertheless, primary twins can be twinned again up to three more times in the present alloy for coarse grains. This feature highlights an original behavior where secondary/tertiary twinning is facilitated compared to the nucleation of new primary twins. Moreover, secondary twins here completely consume the primary twins, resulting in a loss of the primary twinning relationship with the matrix and making their identification difficult. This can particularly lead to a misinterpretation because the OR between the α" matrix and the result of primary $\{130\}\langle 310\rangle_{\alpha''}$ twinning + $\langle 211\rangle_{\alpha''}$ reorientation twinning + secondary $\{130\}\langle 310\rangle_{\alpha''}$ twinning is close to a $\{021\}\langle 512\rangle_{\alpha''}$ type II twinning OR. However, a direct nucleation of such a twin is very unlikely to occur because of its high shear and shuffle required [50] compared to the successive activation of simpler twins with very smaller shear and shuffle magnitudes.

Moreover, this unique features of successive twinning within the primary twins can probably be attributed to the higher Zr addition in the Ti-Zr-Nb-Sn system compared with the conventional Ti-Nb-Zr-Sn one [11,12]. But further investigations about the exact role of Zr atoms are required to confirm this hypothesis. Nevertheless, this comparative study suggests that inhibiting the activation of deformation twins can significantly enhance superelastic performance for metastable β titanium alloys. Therefore, this work not only comprehensively interprets the mechanism of superelasticity improvement via grain size refinement strategy as observed in the previous studies of superelastic Ti-based alloys, but also provides guidance for the design of multifunctional Ti-Zr-Nb-Sn biomedical devices.

5. Conclusion

In this work, the plastically deformed microstructures of the solution-treated Ti20122 alloys behaving the same recrystallized texture but a significant difference in grain size are comparatively investigated using cyclic/conventional tensile tests, OM, *in situ* SXRD, EBSD and TEM. A grain size dependent martensitic twinning behavior is evidenced for the first time and discussed. The main conclusions can be summarized as followings:

1. The superelasticity of the Ti20122 alloy decreases from 3.1 % to 2.5 % after ST-700–30 and ST-900–30 thermal treatments because of an increase of the average grain size from 8 μm to 105 μm before deformation.
2. After deformation, the observed residual martensite has the same feature for both grain size materials. In all of the grains, only the CV with the highest transformation strain is detected, in general with only one habit plane variant, but with the two habit plane variants in few grains. However, twins are observed in the coarse grain material, whereas a twinning-free plastic deformation behavior is evidenced in the fine grain material for the first time in strained superelastic Ti-based alloys.
3. Deformation twins are observed in the coarse grain material after 5 % of strain. These twins present an abnormal orientation relationship with the α" matrix due to a novel three-step twinning process: (i) primary $\{130\}<310>_{\alpha''}$ twin nucleates in SIM α" phase, (ii) the primary$\{130\}<310>_{\alpha''}$ twin is then completely reoriented by $a < 211>_{\alpha''}$ type II twinning system, (iii) this reoriented primary martensitic α" twin is further twinned completely by a secondary $\{130\}<310>_{\alpha''}$ twinning. Reorientation of the primary twin is rationalized by transformation strain calculations: $\{130\}<310>_{\alpha''}$ twins are systematically reorientated if their CV does not correspond to the one with the highest transformation strain value with respect to their β phase counterpart.
4. The previous three-step twinning process can be confused with a direct $\{021\}<512>_{\alpha''}$ type II twinning when comparing the orientation relationship between the α" matrix and the resulting product. However, there are several features that clearly exclude the occurrence of such $\{021\}<512>_{\alpha''}$ type II twinning.
5. With strain increasing to 8 %, the previous primary/secondary α" twins are partially twinned with a third $\{130\}<310>_{\alpha''}$ or a $\{110\}<110>_{\alpha''}$ twinning. The same deformation band is then subjected to an unprecedented four-step twinning process.
6. The grain size refinement strategy is shown for the first time to be an efficient way to improve superelasticity by completely suppressing deformation twinning.

CRediT authorship contribution statement

J.J. Gao: Writing – original draft, Methodology, Investigation, Formal analysis, Data curation, Conceptualization. **P. Castany:** Writing – review & editing, Validation, Formal analysis, Conceptualization. **T. Gloriant:** Writing – review & editing, Formal analysis, Conceptualization.

Declaration of competing interest

The authors declare that they have no known competing financial interests or personal relationships that could have appeared to influence the work reported in this paper.

Acknowledgement

This work was financially sponsored by the National Natural Science Foundation of China (No.52301305), China Postdoctoral Science Foundation (No.2024M754158), and Tianjin Natural Science Foundation (No.23JCQNJC00580). The authors also acknowledge the European Synchrotron Radiation Facility (ESRF) for provision of synchrotron radiation facilities under proposal number MA-3956 and would like to thank beam scientist A.Fitch for assistance and support in using beamline ID22.

Supplementary materials

Supplementary material associated with this article can be found, in the online version, at doi:10.1016/j.actamat.2025.121260.

References

[1] D.J. Wever, A.G. Veldhuizen, M.M. Sanders, J.M. Schakenraad, J.R. van Horn, Cytotoxic, allergic and genotoxic activity of a nickel-titanium alloy, Biomaterials 18 (1997) 1115–1120, https://doi.org/10.1016/S0142-9612(97)00041-0.

[2] M. Tahara, T. Kanaya, H.Y. Kim, T. Inamura, H. Hosoda, S. Miyazaki, Heating-induced martensitic transformation and time-dependent shape memory behavior of Ti-Nb-O alloy, Acta Mater. 80 (2014) 317–326, https://doi.org/10.1016/j.actamat.2014.07.012.

[3] A. Ramarolahy, P. Castany, F. Prima, P. Laheurte, I. Péron, T. Gloriant, Microstructure and mechanical behavior of superelastic Ti-24Nb-0.5O and Ti-24Nb-0.5N biomedical alloys, J. Mech. Behav. Biomed. Mater. 9 (2012) 83–90, https://doi.org/10.1016/j.jmbbm.2012.01.017.

[4] Q. Li, D. Ma, J. Li, M. Niinomi, M. Nakai, Y. Koizumi, D. Wei, T. Kakeshita, T. Nakano, A. Chiba, K. Zhou, D. Pan, Low Young's modulus Ti-Nb-O with high strength and good plasticity, Mater. Trans 59 (2018) 858–860, https://doi.org/10.2320/matertrans.M2018021.

[5] P. Castany, A. Ramarolahy, F. Prima, P. Laheurte, C. Curfs, T. Gloriant, *In situ* synchrotron X-ray diffraction study of the martensitic transformation in superelastic Ti-24Nb-0.5N and Ti-24Nb-0.5O alloys, Acta Mater. 88 (2015) 102–111, https://doi.org/10.1016/j.actamat.2015.01.014.

[6] K. Chou, N. Li, E.A. Marquis, Enhanced work hardening from oxygen-stabilized ω precipitates in an aged metastable β Ti-Nb alloy, Acta Mater. 220 (2021) 117302, https://doi.org/10.1016/j.actamat.2021.117302.

[7] J. Zhang, F. Sun, Y. Hao, N. Gozdecki, E. Lebrun, P. Vermaut, R. Portier, T. Gloriant, P. Laheurte, F. Prima, Influence of equiatomic Zr/Nb substitution on superelastic behavior of Ti-Nb-Zr alloy, Mater. Sci. Eng: A 563 (2013) 78–85, https://doi.org/10.1016/j.msea.2012.11.045.

[8] S. Ozan, J. Lin, Y. Li, R. Ipek, C. Wen, Development of Ti-Nb-Zr alloys with high elastic admissible strain for temporary orthopedic devices, Acta Biomater. 20 (2015) 176–187, https://doi.org/10.1016/j.actbio.2015.03.023.

[9] H.Y. Kim, J. Fu, H. Tobe, J.I. Kim, S. Miyazaki, Crystal structure, transformation strain, and superelastic property of Ti-Nb-Zr and Ti-Nb-Ta alloys, Shap. Mem. Superelast. 1 (2015) 107–116, https://doi.org/10.1007/s40830-015-0022-3.

[10] K. Munir, J. Lin, P.F.A. Wright, S. Ozan, Y. Li, C. Wen, Mechanical, corrosion, nanotribological, and biocompatibility properties of equal channel angular pressed Ti-28Nb-35.4Zr alloys for biomedical applications, Acta Biomater. 149 (2022) 387–398, https://doi.org/10.1016/j.actbio.2022.07.005.

[11] N. Church, C. Talbot, J. Miller, L. Connor, S. Michalik, N. Jones, Evidence of dislocation dependent behaviour in superelastic Ti2448 (Ti-24Nb-4Zr-8Sn, wt %), Acta Mater 255 (2023) 119066, https://doi.org/10.1016/j.actamat.2023.119066.

[12] Q. Liang, D. Wang, Y. Zheng, S. Zhao, Y. Gao, Y. Hao, R. Yang, D. Banerjee, H. L. Fraser, Y. Wang, Shuffle-nanodomain regulated strain glass transition in Ti-24Nb-4Zr-8Sn alloy, Acta Mater. 186 (2020) 415–424, https://doi.org/10.1016/j.actamat.2019.12.056.

[13] H.Y. Kim, Y. Ikehara, J.I. Kim, H. Hosoda, S. Miyazaki, Martensitic transformation, shape memory effect and superelasticity of Ti-Nb binary alloys, Acta Mater. 54 (2006) 2419–2429, https://doi.org/10.1016/j.actamat.2006.01.019.

[14] Y. Yang, P. Castany, M. Cornen, F. Prima, S.J. Li, Y.L. Hao, T. Gloriant, Characterization of the martensitic transformation in the superelastic Ti-24Nb-4Zr-8Sn alloy by *in situ* synchrotron X-ray diffraction and dynamic mechanical analysis, Acta Mater. 88 (2015) 25–33, https://doi.org/10.1016/j.actamat.2015.01.039.

[15] L. López Pavón, H.Y. Kim, H. Hosoda, S. Miyazaki, Effect of Nb content and heat treatment temperature on superelastic properties of Ti-24Zr-(8-12)Nb-2Sn alloys, Scr. Mater. 95 (2015) 46–49, https://doi.org/10.1016/j.scriptamat.2014.09.029.

[16] J. Fu, A. Yamamoto, H.Y. Kim, H. Hosoda, S. Miyazaki, Novel Ti-base superelastic alloys with large recovery strain and excellent biocompatibility, Acta Biomater. 17 (2015) 56–67, https://doi.org/10.1016/j.actbio.2015.02.001.

[17] J.J. Gao, P. Castany, T. Gloriant, Synthesis and characterization of a new TiZrHfNbTaSn high-entropy alloy exhibiting superelastic behavior, Scr. Mater. 198 (2021) 113824, https://doi.org/10.1016/j.scriptamat.2021.113824.

[18] J.J. Gao, I. Thibon, D. Laillé, P. Castany, T. Gloriant, Influence of texture and transformation strain on the superelastic performance of a new Ti-20Zr-3Mo-3Sn alloy, Mater. Sci. Eng: A 762 (2019) 138075, https://doi.org/10.1016/j.msea.2019.138075.

[19] J.J. Gao, I. Thibon, P. Castany, T. Gloriant, Effect of grain size on the recovery strain in a new Ti-20Zr-12Nb-2Sn superelastic alloy, Mater. Sci. Eng: A 793 (2020) 139878, https://doi.org/10.1016/j.msea.2020.139878.

[20] S. Li, M.-S. Choi, T.-H. Nam, Phase stability of the amorphous phase and non-equilibrium phase in a β Ti-Zr-based shape memory alloy, Scr. Mater. 195 (2021) 113721, https://doi.org/10.1016/j.scriptamat.2021.113721.

[21] W. Tasaki, K. Nakano, Y. Sato, T. Koyano, S. Miyazaki, H.Y. Kim, Effects of Zr and Hf on superelasticity, shape memory effect and microstructure of *β*-type (Ti-Zr-Hf)-Nb-Sn multi-principal element alloys with low magnetic susceptibility, Mater. Sci. Eng: A 908 (2024) 146760, https://doi.org/10.1016/j.msea.2024.146760.

[22] H.Y. Kim, T. Sasaki, K. Okutsu, J.I. Kim, T. Inamura, H. Hosoda, S. Miyazaki, Texture and shape memory behavior of Ti-22Nb-6Ta alloy, Acta Mater. 54 (2006) 423–433, https://doi.org/10.1016/j.actamat.2005.09.014.

[23] J.X. Zhang, J.Y. Zhang, W.C. Xiao, J.X. Hou, Q. Li, B. Xiao, S.Y. Yang, J.L. Wu, T. L. Zhang, T. Yang, Grain refinement induced unusually large shape memory effect in lightweight titanium alloy, Acta Mater. 272 (2024) 119936, https://doi.org/10.1016/j.actamat.2024.119936.

[24] J. Wang, W. Xiao, Y. Fu, L. Ren, C. Ma, Dependence of mechanical behavior on grain size of metastable Ti-Nb-O titanium alloy, Prog. Nat. Sci: Mater. Inter. 32 (2022) 63–71, https://doi.org/10.1016/j.pnsc.2021.09.011.

[25] Z.J. Gu, Y.Z. Tian, W. Xu, S. Lu, X.L. Shang, J.W. Wang, G.W. Qin, Optimizing transformation-induced plasticity in CoCrNi alloys by combined grain refinement and chemical tuning, Scr. Mater. 214 (2022) 114658, https://doi.org/10.1016/j.scriptamat.2022.114658.

[26] N. Church, C. Talbot, G. Wise, O. Shah, N. Jones, Development of ultra-high strength Ti-Nb-Sn alloys through grain-refinement by *in situ* Zener pinning, Scr. Mater. 218 (2022) 114809, https://doi.org/10.1016/j.scriptamat.2022.114809.

[27] M. Liu, W. Gong, R. Zheng, J. Li, Z. Zhang, S. Gao, C. Ma, N. Tsuji, Achieving excellent mechanical properties in type 316 stainless steel by tailoring grain size in homogeneously recovered or recrystallized nanostructures, Acta Mater 226 (2022) 117629, https://doi.org/10.1016/j.actamat.2022.117629.

[28] L. Gu, A. Meng, X. Chen, Y. Zhao, Simultaneously enhancing strength and ductility of HCP titanium via multi-modal grain induced extra dislocation hardening, Acta Mater. 252 (2023) 118949, https://doi.org/10.1016/j.actamat.2023.118949.

[29] T. Sun, Z. Shang, J. Cho, J. Ding, T. Niu, Y. Zhang, B. Yang, D. Xie, J. Wang, H. Wang, X. Zhang, Ultra-fine-grained and gradient FeCrAl alloys with outstanding work hardening capability, Acta Mater. 215 (2021) 117049, https://doi.org/10.1016/j.actamat.2021.117049.

[30] B. Zhang, M. Huang, Y. Chong, W. Mao, W. Gong, R. Zheng, Y. Bai, D. Wang, Q. Sun, Y. Wang, N. Tsuji, Achieving large super-elasticity through changing relative easiness of deformation modes in Ti-Nb-Mo alloy by ultra-grain refinement, Mater. Res. Lett. 9 (2021), https://doi.org/10.1080/21663831.2021.1875080.

[31] S.J. Li, M.T. Jia, F. Prima, Y.L. Hao, R. Yang, Improvements in nonlinear elasticity and strength by grain refinement in a titanium alloy with high oxygen content, Scr. Mater. 64 (2011) 1015–1018, https://doi.org/10.1016/j.scriptamat.2011.02.006.

[32] H. Chen, F. Xiao, X. Liang, Z. Li, Z. Li, X. Jin, N. Min, T. Fukuda, Improvement of the stability of superelasticity and elastocaloric effect of a Ni-rich Ti-Ni alloy by precipitation and grain refinement, Scr. Mater. 162 (2019) 230–234, https://doi.org/10.1016/j.scriptamat.2018.11.024.

[33] F. Sun, S. Nowak, T. Gloriant, P. Laheurte, A. Eberhardt, F. Prima, Influence of a short thermal treatment on the superelastic properties of a titanium-based alloy, Scr. Mate. 63 (2010) 1053–1056, https://doi.org/10.1016/j.scriptamat.2010.07.042.

[34] P. Castany, Y. Yang, E. Bertrand, T. Gloriant, Reversion of a parent $\{130\}\langle310\rangle_{\alpha''}$ martensitic twinning system at the origin of $\{332\}\langle113\rangle_{\beta}$ twins observed in metastable β titanium alloys, Phys. Rev. Lett. 117 (2016) 245501, https://doi.org/10.1103/PhysRevLett.117.245501.

[35] Y. Yang, P. Castany, Y.L. Hao, T. Gloriant, Plastic deformation via hierarchical nano-sized martensitic twinning in the metastable β Ti-24Nb-4Zr-8Sn alloy, Acta Mater 194 (2020) 27–39, https://doi.org/10.1016/j.actamat.2020.04.021.

[36] X. Zhang, S. Wang, J. Wu, J. Sun, Y. Gao, B. He, S.J. Pennycook, ω-strengthened Ti-23Nb alloy with twinning-induced plasticity developed via reverse martensitic transformation, Acta Mater 278 (2024) 120234, https://doi.org/10.1016/j.actamat.2024.120234.

[37] M.J. Lai, C.C. Tasan, D. Raabe, On the mechanism of {332} twinning in metastable β titanium alloys, Acta Mater 111 (2016) 173–186, https://doi.org/10.1016/j.actamat.2016.03.040.

[38] M. Besse, P. Castany, T. Gloriant, Mechanisms of deformation in gum metal TNTZ-O and TNTZ titanium alloys: a comparative study on the oxygen influence, Acta Mater 59 (2011) 5982–5988, https://doi.org/10.1016/j.actamat.2011.06.006.

[39] Y. Yang, P. Castany, E. Bertrand, M. Cornen, J.X. Lin, T. Gloriant, Stress release-induced interfacial twin boundary ω phase formation in a β type Ti-based single crystal displaying stress-induced α'' martensitic transformation, Acta Mater. 149 (2018) 97–107, https://doi.org/10.1016/j.actamat.2018.02.036.

[40] G. Chen, D. Li, Y. Zheng, L. Qi, Stability and growth kinetics of {112} twin embryos in β-Ti alloys, Acta Mater. 263 (2024) 119520, https://doi.org/10.1016/j.actamat.2023.119520.

[41] S.Q. Wu, D.H. Ping, Y. Yamabe-Mitarai, W.L. Xiao, Y. Yang, Q.M. Hu, G.P. Li, R. Yang, $\{112\}\langle111\rangle$Twinning during ω to body-centered cubic transition, Acta Mater. 62 (2014) 122–128, https://doi.org/10.1016/j.actamat.2013.09.040.

[42] T. Yao, K. Du, H. Wang, Z. Huang, C. Li, L. Li, Y. Hao, R. Yang, H. Ye, *In situ* scanning and transmission electron microscopy investigation on plastic deformation in a metastable β titanium alloy, Acta Mater. 133 (2017) 21–29, https://doi.org/10.1016/j.actamat.2017.05.018.

[43] E. Bertrand, P. Castany, Y. Yang, E. Menou, T. Gloriant, Deformation twinning in the full-α″ martensitic Ti-25Ta-20Nb shape memory alloy, Acta Mater. 105 (2016) 94–103, https://doi.org/10.1016/j.actamat.2015.12.001.

[44] H.J. Lee, J.H. Kim, C.H. Park, J.-K. Hong, J.-T. Yeom, T. Lee, S.W. Lee, Twinning-induced plasticity mechanism of α''-martensitic titanium alloy, Acta Mater. 248 (2023) 118763, https://doi.org/10.1016/j.actamat.2023.118763.

[45] B. Chen, W. Sun, Transitional structure of $\{332\}\langle113\rangle_{\beta}$ twin boundary in a deformed metastable β-type Ti-Nb-based alloy, revealed by atomic resolution electron microscopy, Scr. Mater. 150 (2018) 115–119, https://doi.org/10.1016/j.scriptamat.2018.03.009.

[46] J.J. Gao, P. Castany, T. Gloriant, Complex multi-step martensitic twinning process during plastic deformation of the superelastic Ti-20Zr-3Mo-3Sn alloy, Acta Mater 236 (2022) 118140, https://doi.org/10.1016/j.actamat.2022.118140.

[47] Y.W. Chai, H.Y. Kim, H. Hosoda, S. Miyazaki, Self-accommodation in Ti-Nb shape memory alloys, Acta Mater. 57 (2009) 4054–4064, https://doi.org/10.1016/j.actamat.2009.04.051.

[48] Y.W. Chai, H.Y. Kim, H. Hosoda, S. Miyazaki, Interfacial defects in Ti-Nb shape memory alloys, Acta Mater 56 (2008) 3088–3097, https://doi.org/10.1016/j.actamat.2008.02.045.

[49] E. Bertrand, P. Castany, I. Péron, T. Gloriant, Twinning system selection in a metastable β-titanium alloy by Schmid factor analysis, Scr. Mater. 64 (2011) 1110–1113, https://doi.org/10.1016/j.scriptamat.2011.02.033.

[50] H. Tobe, H.Y. Kim, T. Inamura, H. Hosoda, S. Miyazaki, Origin of {332} twinning in metastable β-Ti alloys, Acta Mater. 64 (2014) 345–355, https://doi.org/10.1016/j.actamat.2013.10.048.

[51] R. Zheng, W. Gong, J. Du, S. Gao, M. Liu, G. Li, T. Kawasaki, S. Harjo, C. Ma, S. Ogata, N. Tsuji, Rediscovery of Hall-Petch strengthening in bulk ultrafine grained pure Mg at cryogenic temperature: a combined *in-situ* neutron diffraction and electron microscopy study, Acta Mater. 238 (2022) 118243, https://doi.org/10.1016/j.actamat.2022.118243.

[52] Y. Jiang, S. Li, N. Liang, S. Lan, Y. Zhang, W. Yin, G. Sha, S. Divinski, G. Wilde, J. T. Wang, Revealing the high strength and high thermal stability of a nano-lamellar Cu-0.1 at. % Zr alloy, Acta Mater. 276 (2024) 120163, https://doi.org/10.1016/j.actamat.2024.120163.

[53] Y.D. Im, Y.K. Lee, H.K. Park, K.H. Song, Effect of the initial grain size and orientation on the formation of deformation twins in Ti-15Mo alloy, J. Mater. Sci. 52 (2017) 11668–11674, https://doi.org/10.1007/s10853-017-1314-0.

[54] K. Yao, X. Min, Static and dynamic Hall−Petch relations in $\{332\}\langle113\rangle$TWIP Ti-15Mo alloy, Mater. Sci. Eng: A 827 (2021) 142044, https://doi.org/10.1016/j.msea.2021.142044.

[55] A. Ghaderi, M.R. Barnett, Sensitivity of deformation twinning to grain size in titanium and magnesium, Acta Mater. 59 (2011) 7824–7839, https://doi.org/10.1016/j.actamat.2011.09.018.

[56] K.M. Rahman, V.A. Vorontsov, D. Dye, The effect of grain size on the twin initiation stress in a TWIP steel, Acta Mater. 89 (2015) 247–257, https://doi.org/10.1016/j.actamat.2015.02.008.

[57] I. Gutierrez-Urrutia, S. Zaefferer, D. Raabe, The effect of grain size and grain orientation on deformation twinning in a Fe-22wt. % Mn-0.6wt.% C TWIP steel, Mater. Sci. Eng. A 527 (2010) 3552–3560, https://doi.org/10.1016/j.msea.2010.02.041.

[58] S.J. Sun, Y.Z. Tian, H.R. Lin, H.J. Yang, X.G. Dong, Y.H. Wang, Z.F. Zhang, Transition of twinning behavior in CoCrFeMnNi high entropy alloy with grain refinement, Mater. Sci. Eng: A 712 (2018) 603–607, https://doi.org/10.1016/j.msea.2017.12.022.

[59] C. Wagner, G. Laplanche, Effect of grain size on critical twinning stress and work hardening behavior in the equiatomic CrMnFeCoNi high-entropy alloy, Int. J. Plast. 166 (2023) 103651, https://doi.org/10.1016/j.ijplas.2023.103651.

[60] X. Huang, J.S. Li, M.J. Lai, Influences of grain size on the deformation behavior of a twinning-induced plasticity metastable β titanium alloy, J. Alloys Comp. 937 (2023) 168274, https://doi.org/10.1016/j.jallcom.2022.168274.

[61] W.L. Wang, X.L. Wang, W. Mei, J. Sun, Role of grain size in tensile behavior in twinning-induced plasticity β Ti-20V-2Nb-2Zr alloy, Mater. Char. 120 (2016) 263–267, https://doi.org/10.1016/j.matchar.2016.09.016.

[62] M.F. Ashby, The deformation of plastically non-homogeneous materials, Philos. Mag. A 21 (1970) 399–424, https://doi.org/10.1080/14786437008238426.

[63] Y. Guo, D.M. Collins, E. Tarleton, F. Hofmann, A.J. Wilkinson, T.B. Britton, Dislocation density distribution at slip band-grain boundary intersections, Acta Mater. 182 (2020) 172–183, https://doi.org/10.1016/j.actamat.2019.10.031.